Computer Methods in Applied Mechanics and Engineering 458 (2026) 119073

Contents lists available at ScienceDirect

Comput. Methods Appl. Mech. Engrg.

journal homepage: www.elsevier.com/locate/cma

Salt cavern simulations with a stabilized mixed finite element formulation for low-order tetrahedral elements

Hermínio T. Honório [a,b,*], Andrea Franceschini [c], Massimiliano Ferronato [c], Hadi Hajibeygi [b]

[a] TNO-GDN Geological Survey of the Netherlands, 3584CB Utrecht, The Netherlands
[b] Faculty of Civil Engineering and Geosciences, Delft University of Technology, Stevinweg 1, 2628CN, Delft, The Netherlands
[c] Dept. of Civil, Environmental and Architectural Engineering, University of Padova, Padova, Italy

ARTICLE INFO

Dataset link: repository

Keywords:
Salt caverns
Mixed finite elements
Stabilization
Tetrahedral meshes
Oscillations

ABSTRACT

Salt cavern simulations involve many numerical challenges that need to be addressed in order to ensure accurate and meaningful results. Firstly, lithological structures and solution-mined salt caverns always present fairly complex shapes, which favors the use of tetrahedral meshes with local refinements for adequate domain discretization. Secondly, salt rocks are known to creep under deviatoric stresses, meaning that deformations take place at constant volume (isochoric). The combination of isochoric deformations with tetrahedral meshes is particularly problematic for low-order finite element formulations. This work presents a stabilized mixed finite element (FE) formulation for linear tetrahedrons, where the mean stress is a primary variable, incorporating all the relevant deformation mechanisms for salt rocks. The stabilization consists of enriching the displacement FE approximation in the mean stress equation by obtaining an approximation for the Laplacian of the displacement that accounts for inelastic strains. This is achieved by using the Physical Influence Scheme (PIS) with the concept of secant Young's modulus, which promotes local stabilizations where necessary. When combined with a proper calculation of a geometric parameter h, this stabilization technique is shown to produce oscillation-free and physically consistent results without any sort of tuning parameter. The proposed technique is analyzed in relevant test cases for salt cavern simulations and the results show the effectiveness of the proposed stabilization to eliminate spurious numerical oscillations with low-order tetrahedral meshes.

1. Introduction

Simulating the mechanical behavior of salt caverns is an important step to ensure mechanical stability during the entire cavern's life cycle, i.e., from leaching to storage operation and after abandonment [1]. While accurate stress calculations are crucial for stability assessment, they are also challenging for many reasons including e.g. complexities within the lithological descriptions, uncertainties associated with initial stress conditions, use of adequate and properly calibrated constitutive models, and numerical accuracy and stability of the simulations [2,3]. The present work focuses on the numerical aspects of stress calculations in salt caverns as it relates to relevant constitutive models for salt rocks.

Salt rocks exhibit a complex time-dependent mechanical behavior with different deformation mechanisms taking place simultaneously. When a constant differential stress is applied, a salt rock immediately responds elastically with a subsequent time-dependent

* Corresponding author at: TNO-GDN Geological Survey of the Netherlands, 3584CB Utrecht, The Netherlands.
E-mail address: herminio.tasinafohonorio@tno.nl (H.T. Honório).

https://doi.org/10.1016/j.cma.2026.119073
Received 10 February 2026; Received in revised form 6 May 2026; Accepted 7 May 2026
Available online 14 May 2026

inelastic response with a high strain rate. As time progresses, the strain rate slowly decreases, thus characterizing the transient (or primary) creep stage. The steady-state creep stage is defined after the strain rate stabilizes at a constant value. This stage is well described in the literature, for which two different mechanisms are commonly considered. The first one is dislocation creep, which occurs by a rearrangement of the crystal lattice internally to the salt grains, and has a non-linear dependency with stress. The second one is a fluid assisted deformation mechanism that consists of dissolution of salt around grain regions of high pressure and precipitation in low pressure regions. This mechanism is commonly referred to as pressure solution creep, which is highly dependent on grain size, and has linear dependency with stress. It is widely recognized that dislocation creep dominates at high differential stresses, while low differential stresses have a greater effect on pressure solution creep. Moreover, salt behavior is strongly dependent on whether the stress condition lies in the compressibility or dilatancy regions. In the compressibility region, salt presents transient and steady-state creep and continually deforms without failure. On the other hand, if the material operates in the dilatancy region, micro-cracks start to form and accumulate, occupying space (volumetric increase) and weakening the material, thus causing tertiary creep to appear. This tertiary creep stage is characterized by a rapid increase in strain rate followed by brittle failure of the rock. Other mechanisms, such as reverse transient creep and thermal strains might also play a role in salt cavern operations. In addition to thermal strains, temperature variations can significantly affect creep behavior. Therefore, including thermal effects is also important for accurate predictions of the mechanical behavior of salt caverns.

As exposed in the previous paragraph, creep is an essential mechanism to be described by any the constitutive model for salt rocks. Dislocation and pressure solution creep mechanisms are particularly important for the long term behavior of salt caverns. These two mechanisms are exclusively dependent on the deviatoric stresses–in other words, they are J_2-dependent viscoplastic models. It is well-known that J_2 (visco)plasticity, such as the classical power-law formulations for dislocation and pressure solution creep, produce isochoric deformations, which in practice induce an incompressibility constraint to the system. As a result, non-physical numerical oscillations appear in the mean stress field due to locking. Such mean stress oscillations suggest the use of a mixed displacement-mean stress formulation with a choice of the pair of approximation spaces satisfying the Ladyzhenskaya–Babuška–Brezzi (LBB) stability condition [4]. This implies that classical low-order P1-P1 mixed elements are also prone to numerical instabilities, unless a stabilization technique is employed. Many stabilization techniques have been devised in the literature to address problems with incompressibility constraints, such as Stokes flows [5–7], incompressible Navier–Stokes [5,8,9], linear elasticity for (nearly-)incompressible materials [10–12], coupled poroelasticity [13–19], etc. These problems share the same saddle-point structure that cause instability issues when combined with interpolation pairs not satisfying LBB condition. This is also the case for isochoric (i.e., J_2) plasticity, for which some of the previous stabilization strategies have been adapted to. For instance, the sub-grid scale approach, initially proposed in [20], was extended to incompressible (i.e. J_2) plasticity in [21]. In [22], the effects of softening in strain localizations are investigated, where the authors compare the orthogonal sub-grid scale (OSGS) with the Galerkin least-square (GLS). In the same work [22], the authors propose two local stabilization strategies based on (i) secant shear modulus and (ii) on a consistent residual viscosity. Similarly, the stabilization parameter proposed in [5] is modified in [23] to account for plasticity. The concept of secant (or effective) shear modulus was also used as a scaling factor for the stabilization parameters obtained from the variational multiscale method in [24]. Although much attention has been given to J_2-plasticity, inelastic and viscoelastic volumetric strains can also cause mild mean stress oscillations, as will be shown in the present work. These two types of volumetric strains may be present in salt rocks, but the formulations proposed in the literature do not account for these terms.

It is important to keep in mind that locking issues could potentially be avoided by using hexahedral meshes, in which displacement-based B-Bar [25] (or F-Bar [26], for large deformations) methods, for example, can be applied. However, lithological structures and salt cavern shapes can be highly complex, thus making the construction of hexahedral meshes considerably challenging. In [27], for instance, the authors dedicate an entire paper for describing a methodology for building hexahedral meshes for systems of caverns with complex shapes. From a geometrical/discretization point of view, algorithms to generate tetrahedral meshes are much more advanced, requiring much less human intervention than hexahedral meshes. In this context, tetrahedral meshes are unquestionably preferable for discretizing complex geological structures. From a numerical perspective, however, ensuring accurate results with tetrahedral meshes can be much more challenging.

Taking into account the mechanical behavior of salt rocks and the possibility of dealing with complex geometries, the present work proposes a mixed finite element formulation for linear tetrahedral meshes able to handle general constitutive models. The formulation incorporates the effects of inelastic and viscoelastic volumetric strains, which are present in salt rocks, in addition to J_2-viscoplastic deformations. The mixed formulation is obtained through the classical decomposition of the stress tensor into its deviatoric and spherical (i.e., mean stress) parts. The volumetric strains are properly accounted for in the mean stress equation. To avoid spurious oscillations, stabilization terms are introduced into the mean stress equation by enriching the finite element approximation for the displacement field. Following the ideas proposed in [19], the displacement enrichment is achieved by a combination of the Physical Influence Scheme (PIS) and a proper calculation of a geometric parameter h, which is commonly referred to as a characteristic length of the element. Finally, inspired by the concept of secant shear modulus presented in [22], PIS is adapted to include the effects of non-elastic (i.e., inelastic plus viscoelastic) strains, which is shown to be crucial to ensure appropriate local stabilization in regions with higher viscoplastic strains.

To present our methodology, we begin by formally defining the mathematical models in Section 2, and the constitutive model in Section 3. Section 4 introduces the stress decomposition and linearization, which are essential to include non-elastic volumetric strain effects into the mechanical formulation. The weak forms of the heat diffusion and mechanical models are presented in Section 5, while Section 6 introduces the finite element approximations as well as the resulting discrete problems. The stabilization method is proposed in Section 7, where two approaches are considered. The outcome from using the proposed stabilization approaches together with the primal displacement-based formulation adopted in [28] is investigated in Section 8 with the aid of a number of test cases exploring different configurations. Finally, Section 9 closes the presentation with some remarks and conclusions.

2. Mathematical model

2.1. Linear momentum equations

Consider a time domain $\tau \in [t_0, t_f]$ and a spatial domain $\Omega \in \mathbb{R}^3$ bounded by a closed surface Γ outward oriented by a normal vector $\hat{\mathbf{n}}$. The bounding surface can be further split into Γ^u (for Dirichlet boundary conditions) and Γ^σ (for Neumann boundary conditions), such that $\Gamma = \Gamma^u \cup \Gamma^\sigma$ and $\Gamma^u \cap \Gamma^\sigma = \emptyset$. The linear momentum balance equation for quasi-static loads can be written as

$$-\nabla \cdot \boldsymbol{\sigma} = \mathbf{b} \quad \forall \quad (\mathbf{x}, t) \in (\Omega \times \tau), \tag{1}$$

where $\boldsymbol{\sigma}$ is the rank-2 stress tensor and $\mathbf{b}$ is the vector of body forces. Eq. (1) is subjected to the following boundary and initial conditions:

$$\mathbf{u}(\mathbf{x}, t) = \bar{\mathbf{u}}(\mathbf{x}, t) \quad \forall \quad (\mathbf{x}, t) \in (\Gamma^u \times \tau) \tag{2}$$

$$\boldsymbol{\sigma}(\mathbf{x}, t) \cdot \hat{\mathbf{n}} = \bar{\mathbf{t}}(\mathbf{x}, t) \quad \forall \quad (\mathbf{x}, t) \in (\Gamma^\sigma \times \tau) \tag{3}$$

$$\boldsymbol{\sigma}(\mathbf{x}, t_0) = \boldsymbol{\sigma}_0(\mathbf{x}) \quad \forall \quad \mathbf{x} \in \Omega \tag{4}$$

where $\bar{\mathbf{u}}(\mathbf{x}, t)$ and $\bar{\mathbf{t}}(\mathbf{x}, t)$ are the displacement and traction vector functions prescribed at Γ^u and Γ^σ, respectively, and $\boldsymbol{\sigma}_0$ is the initial stress tensor field.

By considering small strains, the compatibility equation reads

$$\boldsymbol{\varepsilon}(\mathbf{u}) = \frac{1}{2}\left(\nabla \mathbf{u} + \nabla \mathbf{u}^T\right), \tag{5}$$

where $\mathbf{u}$ denotes the displacement vector. Finally, the stress tensor is related to the strain by Hooke's law:

$$\boldsymbol{\sigma} = \mathbb{C}_e : \boldsymbol{\varepsilon}_e, \tag{6}$$

with $\mathbb{C}_e$ denoting the rank-4 elastic stiffness tensor and $\boldsymbol{\varepsilon}_e$ the rank-2 elastic strain tensor. Calculation of $\boldsymbol{\varepsilon}_e$ depends on the adopted constitutive model, and will be addressed in Section 3.

2.2. Heat diffusion equation

Consider the space–time domain $\Omega \times \tau$ and split the closed surface Γ into Γ^T, Γ^q, and Γ^h, such that $\Gamma = \Gamma^T \cup \Gamma^q \cup \Gamma^h$, and $\Gamma^T \cap \Gamma^q = \Gamma^T \cap \Gamma^h = \Gamma^h \cap \Gamma^q = \emptyset$. The heat diffusion equation without heat generation can be expressed as

$$\rho c \frac{\partial T}{\partial t} - \nabla \cdot (k \nabla T) = 0 \quad \forall \quad (\mathbf{x}, t) \in (\Omega \times \tau), \tag{7}$$

where T is the temperature field, c is the specific heat capacity, ρ is the density, and k is the thermal conductivity. Eq. (7) is subjected to the following boundary and initial conditions:

$$T(\mathbf{x}, t) = \bar{T}(\mathbf{x}, t) \quad \forall \quad (\mathbf{x}, t) \in (\Gamma^T \times \tau) \tag{8}$$

$$-k \nabla T(\mathbf{x}, t) \cdot \hat{\mathbf{n}} = \bar{q}''(\mathbf{x}, t) \quad \forall \quad (\mathbf{x}, t) \in (\Gamma^q \times \tau) \tag{9}$$

$$-k \nabla T(\mathbf{x}, t) \cdot \hat{\mathbf{n}} = h_{\text{conv}}\left(T - T_\infty\right) \quad \forall \quad (\mathbf{x}, t) \in (\Gamma^h \times \tau) \tag{10}$$

$$T(\mathbf{x}, t_0) = T_0(\mathbf{x}) \quad \forall \quad \mathbf{x} \in \Omega \tag{11}$$

where $\bar{T}(\mathbf{x}, t)$ and $\bar{q}''(\mathbf{x}, t)$ are the temperature and heat flux functions prescribed at Γ^T and Γ^q, respectively. Additionally, h_{conv} is the convective heat transfer coefficient, and T_∞ is the far field temperature (usually the gas/brine temperature).

3. Constitutive model

The present work intends to capture transient creep, steady-state creep, and reverse transient creep, which are schematically illustrated in Fig. 1. The constitutive model adopted to represent these mechanisms is an extension of the one used in [28], which originally includes transient creep, reverse transient creep, and steady-state dislocation creep. The extensions proposed in the present work consist of adding thermal strains and pressure solution mechanism for the steady-state creep stage. A schematic representation of the model is shown in Fig. 2, which identifies the elements (mechanical analogs, such as springs and dashpots) responsible for describing each creep deformation mechanism.

By assuming infinitesimal strains, all these elastic ($\boldsymbol{\varepsilon}_e$), non-elastic ($\boldsymbol{\varepsilon}_{ne}$), and thermal ($\boldsymbol{\varepsilon}_{th}$) strains constitute the total strain tensor $\boldsymbol{\varepsilon}$, i.e.,

$$\boldsymbol{\varepsilon} = \boldsymbol{\varepsilon}_e + \boldsymbol{\varepsilon}_{ne} + \boldsymbol{\varepsilon}_{th}, \tag{12}$$

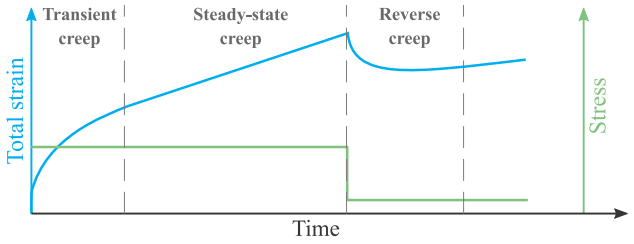

Fig. 1. Creep deformation mechanisms considered in the present work.

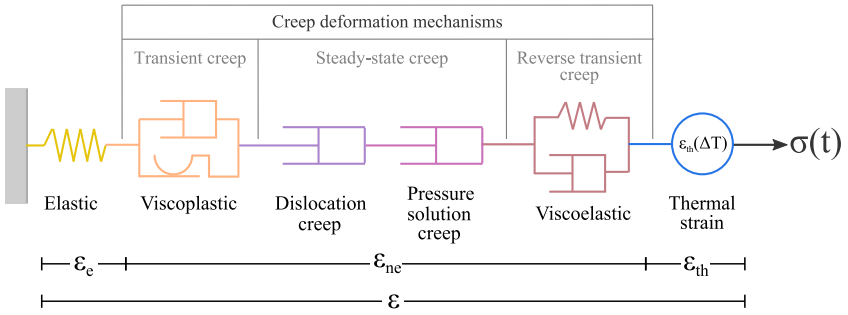

Fig. 2. Constitutive model composition for capturing creep stages plus the thermal response element.

as also shown in Fig. 2. Here, the non-elastic strains comprise all the inelastic elements, $\boldsymbol{\varepsilon}_{ie}$, (i.e., viscoplastic, dislocation, and pressure solution creep elements) and the viscoelastic element, $\boldsymbol{\varepsilon}_{ve}$, such that $\boldsymbol{\varepsilon}_{ne} = \boldsymbol{\varepsilon}_{ie} + \boldsymbol{\varepsilon}_{ve}$. From Eqs. (12) and (6), the stress tensor is written as

$$\boldsymbol{\sigma} = \mathbb{C}_e : \left(\boldsymbol{\varepsilon} - \boldsymbol{\varepsilon}_{ne} - \boldsymbol{\varepsilon}_{th}\right). \tag{13}$$

For the sake of completeness, the models adopted for each element shown in Fig. 2 are briefly described in the following subsections.

In the remainder, we will frequently use the concepts of deviatoric and spherical components of a rank-2 tensor. The symbol $\tilde{}$ is used to indicate the deviatoric part of tensor, and the subscript v to denote its spherical part. For example, a rank-2 tensor $\mathbf{A}$ can be decomposed as

$$\mathbf{A} = \tilde{\mathbf{A}} + A_v \mathbf{I}, \tag{14}$$

where $\tilde{\mathbf{A}}$ is the deviatoric part of $\mathbf{A}$, and $A_v\mathbf{I}$ is its spherical part, with $A_v = \mathrm{tr}(\mathbf{A})/3$ and $\mathbf{I}$ being the rank-2 identity tensor. An exception applies to the spherical part of the stress tensor, which is denoted by p, i.e.,

$$\boldsymbol{\sigma} = \tilde{\boldsymbol{\sigma}} + p\mathbf{I}. \tag{15}$$

3.1. Thermal strain

The thermal strain element is represented in Fig. 2 as a ballon that only responds to temperature variations ΔT, not stress. The thermal strain is given by

$$\boldsymbol{\varepsilon}_{th} = \alpha_{th} \Delta T \ \mathbf{I}, \tag{16}$$

where α_{th} is the thermal expansion coefficient, indicating that thermal strains affect volume without material distortion.

3.2. Viscoelastic model

The viscoelastic model is represented by a Kelvin-Voigt element, which consists of a parallel arrangement between a spring and a dashpot. The stress $\boldsymbol{\sigma}$ applied to this type of element is balanced by the stresses on the spring and the dashpot:

$$\boldsymbol{\sigma} = \underbrace{\mathbb{C}_{ve} : \boldsymbol{\varepsilon}_{ve}}_{\text{spring}} + \underbrace{\eta_{ve}\dot{\boldsymbol{\varepsilon}}_{ve}}_{\text{dashpot}} \quad \rightarrow \quad \dot{\boldsymbol{\varepsilon}}_{ve} = \frac{1}{\eta_{ve}}\left(\boldsymbol{\sigma} - \mathbb{C}_{ve} : \boldsymbol{\varepsilon}_{ve}\right), \tag{17}$$

where $\boldsymbol{\varepsilon}_{ve}$ represents the strain of both spring and dashpot, $\mathbb{C}_{ve}$ is the elastic stiffness rank-4 tensor associated to the spring, and η_{ve} is the dashpot viscosity.

3.3. Dislocation creep model

The dislocation creep mechanism is commonly described by a power-law function together with the Arrhenius law. The expression for the dislocation creep strain rate can be written as

$$\dot{\boldsymbol{\epsilon}}_{ds} = A_{ds} \exp\left(-\frac{Q_{ds}}{RT}\right) q^{n-1} \tilde{\boldsymbol{\sigma}}, \tag{18}$$

where A_{ds} and n are material parameters, Q_{ds} is the activation energy, R is the universal gas constant ($R = 8.32$ J K^{-1} mol^{-1}), and T is the temperature in Kelvin. Additionally, q represents the von Mises stress.

3.4. Pressure solution creep model

Pressure solution creep is characterized by a linear dependency on stress, as opposed to dislocation creep. In addition, it is inversely proportional to the temperature and to the cube of the grain size (diameter). The strain rate is given by

$$\dot{\boldsymbol{\epsilon}}_{ps} = \frac{A_{ps}}{d^3 T} \exp\left(-\frac{Q_{ps}}{RT}\right) \tilde{\boldsymbol{\sigma}}, \tag{19}$$

where A_{ps} is a material parameter, Q_{ps} is the activation energy (in J/mol), and d is the grain size (diameter).

3.5. Viscoplastic model

The viscoplastic element refers to the model proposed in [29] and used in [3,28] for salt caverns. This element can be represented by a parallel arrangement of a dashpot, which represents the time dependency, and a friction element, which indicates that the dashpot will only move if the stress exceeds a certain threshold (the yield surface). As shown in the following, this dashpot also includes a hardening rule that expands the yield surface. The viscoplastic element follows the formulation proposed in [29], that is,

$$\dot{\boldsymbol{\epsilon}}_{vp} = \mu_1 \left\langle \frac{F_{vp}}{F_0} \right\rangle^{N_1} \frac{\partial Q_{vp}}{\partial \boldsymbol{\sigma}}, \tag{20}$$

where μ_1 and N_1 are material parameters, and F_0 is a reference value equal to 1 MPa. The terms F_{vp} and Q_{vp} represent the yield and potential functions, respectively. In this work, only the associative formulation is implemented, that is, $F_{vp} = Q_{vp}$. The yield function is given by

$$F_{vp}(\boldsymbol{\sigma}, \alpha) = J_2 - (-\alpha I_1^n + \gamma I_1^2) \left[\exp(\beta_1 I_1) - \beta \cos(3\psi)\right]^m, \tag{21}$$

where γ, n, β_1, β and m are material parameters. The terms I_1, J_2, and ψ respectively denote the first stress invariant of $\boldsymbol{\sigma}$, the second stress invariant of $\tilde{\boldsymbol{\sigma}}$, and Lode's angle. Finally, α represents the internal hardening parameter, whose role is to expand the yield surface as the inelastic strain (ξ) accumulates in the material. The evolution equation for the hardening parameter used in this work has the following structure:

$$\alpha = a_1 \left[\left(\frac{a_1}{\alpha_0}\right)^{1/\eta} + \xi\right]^{-\eta}, \tag{22}$$

where a_1 and η are material parameters, α_0 is the initial hardening parameter, and the accumulated inelastic strain is given by

$$\xi = \int_{t_0}^{t} \sqrt{\dot{\boldsymbol{\epsilon}}_{vp} : \dot{\boldsymbol{\epsilon}}_{vp}} \mathrm{dt}. \tag{23}$$

The initial hardening parameter can be chosen arbitrarily or based on a specific value of F_{vp}. For a certain value F_{vp}^*, for example, the initial hardening parameter can be computed as

$$\alpha_0 = \gamma I_1^{2-n} + \frac{F_{vp}^* - J_2}{I_1^n} \left[\exp(\beta_1 I_1) + \beta \cos(3\psi)\right]. \tag{24}$$

If the stress state is set at the onset of viscoplasticity, we have $F_{vp}^* = 0$.

It is important to notice that this viscoplastic model is not proven to be thermodynamically consistent for all ranges of stresses and material parameters [29]. Here, we assume the model satisfies the laws of thermodynamics in the conditions of our applications. A rigorous thermodynamic analysis is indeed necessary to validate our assumption. Nevertheless, this viscoplastic model is adopted here specifically because of its dependency on I_1, which results in the representation of the inelastic volumetric strains in our model. One of the main goals of the present study is to investigate the performance of our proposed formulation in the presence of such inelastic volumetric strains.

3.6. Non-elastic strain rate

The time dependent elements in the constitutive model shown in Fig. 2 have expressions for the strain rates (see Eqs. (17) through (20)), rather than the strains. It is therefore convenient to group these expressions in a "total" non-elastic strain rate, that is,

$$\dot{\boldsymbol{\epsilon}}_{ne} = \dot{\boldsymbol{\epsilon}}_{ve} + \dot{\boldsymbol{\epsilon}}_{ds} + \dot{\boldsymbol{\epsilon}}_{ps} + \dot{\boldsymbol{\epsilon}}_{vp}. \tag{25}$$

To calculate the stress, Eq. (25) must first be integrated in time to obtain an expression for $\boldsymbol{\epsilon}_{ne}$, as requested by Eq. (13). Moreover, we notice that $\dot{\boldsymbol{\epsilon}}_{ne}$, and thus $\boldsymbol{\epsilon}_{ne}$, also depend on the stress, which makes the problem non-linear. Therefore, the second step is to linearize these expressions. These two steps are described in the following section.

4. Linearized equations

The constitutive model employed in this work is highly non-linear, thus requiring a proper linearization of the governing equations in order to obtain the model solution. The linearization process starts with obtaining a linearized expression for the stress tensor, considering the split shown in Eq. (15), and subsequent linearization of the momentum and mean stress equations. This process is described in this section. After the governing equations are linearized, the following sections present their corresponding weak forms (Section 5) and finite element approximations (Section 6).

4.1. Stress linearization

The mixed formulation is obtained by splitting the stress tensor ($\boldsymbol{\sigma}$) into its spherical and deviatoric ($\tilde{\boldsymbol{\sigma}}$) parts (see Eq. (15)), such that the mean stress p is treated as a primary unknown of the problem. The deviatoric stress depends on the deviatoric elastic strain tensor, $\tilde{\boldsymbol{\epsilon}}_e$, as

$$\tilde{\boldsymbol{\sigma}} = 2G\,\tilde{\boldsymbol{\epsilon}}_e = 2G\left(\tilde{\boldsymbol{\epsilon}} - \tilde{\boldsymbol{\epsilon}}_{ne}\right), \tag{26}$$

with G denoting the shear modulus. Note that the deviatoric part of the thermal strain tensor $\boldsymbol{\epsilon}_{th}$ is zero. The deviatoric strain tensor contributions $\tilde{\boldsymbol{\epsilon}}$ and $\tilde{\boldsymbol{\epsilon}}_{ne}$ read

$$\tilde{\boldsymbol{\epsilon}} = \boldsymbol{\epsilon} - \frac{1}{3}\epsilon_v \mathbf{I} = \frac{1}{2}\left(\nabla\mathbf{u} + \nabla\mathbf{u}^T\right) - \frac{1}{3}\left(\nabla\cdot\mathbf{u}\right)\mathbf{I}, \tag{27}$$

$$\tilde{\boldsymbol{\epsilon}}_{ne} = \boldsymbol{\epsilon}_{ne} - \frac{1}{3}\epsilon_{ne,v}\mathbf{I}. \tag{28}$$

In what follows, we show how to conveniently express $\boldsymbol{\epsilon}_{ne}$ and $\epsilon_{ne,v}$, so that Eq. (28) can be appropriately evaluated. Performing a time integration of the non-elastic strain rates of Eq. (25) between t and $t+\Delta t$ and using the $\theta-$method to approximate the integral lead to

$$\boldsymbol{\epsilon}_{ne} = \boldsymbol{\epsilon}^t_{ne} + \phi_1\dot{\boldsymbol{\epsilon}}^t_{ne} + \phi_2\dot{\boldsymbol{\epsilon}}_{ne}, \tag{29}$$

with $\phi_1 = (1-\theta)\Delta t$, $\phi_2 = \theta\Delta t$, and $\theta \in [0,1]$ with $\theta = 0, 0.5, 1$ providing the explicit Euler, Crank–Nicolson, and implicit Euler methods, respectively. Moreover, the superscript t denotes the quantities evaluated at the previous time level t, and no superscript is used for quantities evaluated at the current time level $t+\Delta t$.

The challenge in Eq. (29) is to evaluate the non-elastic strain rate at the current time level ($\dot{\boldsymbol{\epsilon}}_{ne}$) as it depends on the stress tensor, thus requiring non-linear iterations to be performed within each time level. For this purpose, we use Taylor series to expand the non-elastic strain rate from iteration k to $k+1$, as done in [28]. In general, the non-elastic strain rate depends on the stress tensor $\boldsymbol{\sigma}$ and on a vector of internal variables, $\mathbf{s}$, such that $\dot{\boldsymbol{\epsilon}}^{k+1}_{ne}$ can be expanded as:

$$\dot{\boldsymbol{\epsilon}}^{k+1}_{ne} = \dot{\boldsymbol{\epsilon}}^{k}_{ne} + \frac{\partial\dot{\boldsymbol{\epsilon}}^{k}_{ne}}{\partial\boldsymbol{\sigma}} : \delta\boldsymbol{\sigma} + \frac{\partial\dot{\boldsymbol{\epsilon}}^{k}_{ne}}{\partial\mathbf{s}}\cdot\delta\mathbf{s}, \tag{30}$$

with $\delta\boldsymbol{\sigma} = \boldsymbol{\sigma}^{k+1} - \boldsymbol{\sigma}^k$ and $\delta\mathbf{s} = \mathbf{s}^{k+1} - \mathbf{s}^k$. The variation of the internal variables is governed by a set of evolution equations, $\mathbf{r}(\boldsymbol{\sigma},\mathbf{s}) = 0$, which allow us to express the increment $\delta\mathbf{s}$ as a function of $\delta\boldsymbol{\sigma}$. Since the evolution equations are generally highly non-linear, the relationship between $\delta\mathbf{s}$ and $\delta\boldsymbol{\sigma}$ can be obtained by expanding also $\mathbf{r}^{k+1}$ around $\mathbf{r}^k$, getting:

$$\delta\mathbf{s} = -\left[\frac{\partial\mathbf{r}^k}{\partial\mathbf{s}}\right]^{-1}\left(\mathbf{r}^k + \frac{\partial\mathbf{r}^k}{\partial\boldsymbol{\sigma}} : \delta\boldsymbol{\sigma}\right). \tag{31}$$

Introducing Eq. (31) into Eq. (30) results in

$$\dot{\boldsymbol{\epsilon}}^{k+1}_{ne} = \dot{\boldsymbol{\epsilon}}^{k}_{ne} + \mathbb{G}^k_{ne} : \delta\boldsymbol{\sigma} - \mathbf{B}^k_{ne}, \tag{32}$$

with:

$$\mathbb{G}^k_{ne} = \frac{\partial\dot{\boldsymbol{\epsilon}}^{k}_{ne}}{\partial\boldsymbol{\sigma}} - \frac{\partial\dot{\boldsymbol{\epsilon}}^{k}_{ne}}{\partial\mathbf{s}}\cdot\left[\frac{\partial\mathbf{r}^k}{\partial\mathbf{s}}\right]^{-1}\frac{\partial\mathbf{r}^k}{\partial\boldsymbol{\sigma}}, \tag{33}$$

$$\mathbf{B}^k_{ne} = \frac{\partial\dot{\boldsymbol{\epsilon}}^{k}_{ne}}{\partial\mathbf{s}}\cdot\left[\frac{\partial\mathbf{r}^k}{\partial\mathbf{s}}\right]^{-1}\mathbf{r}^k. \tag{34}$$

See [28] for full derivation.

To simplify the notation, we suppress the superscript $k+1$ from the variables evaluated at the current non-linear iteration level. Substituting Eq. (32) into Eq. (29) yields the following expression for the non-elastic strain at iteration $k+1$:

$$\boldsymbol{\varepsilon}_{ne} = \boldsymbol{\varepsilon}^{k}_{ne} + \phi_2 \mathbb{G}^{k}_{ne} : \delta\boldsymbol{\sigma} - \phi_2 \mathbf{B}^{k}_{ne}, \tag{35}$$

where $\boldsymbol{\varepsilon}^{k}_{ne} = \boldsymbol{\varepsilon}^{t}_{ne} + \phi_1 \dot{\boldsymbol{\varepsilon}}^{t}_{ne} + \phi_2 \dot{\boldsymbol{\varepsilon}}^{k}_{ne}$.

While the non-elastic volumetric strain $\varepsilon_{ne,v}$ is zero in J_2-plasticity and could be readily removed from Eq. (28), as performed in [24], it can be non-zero according to the constitutive model shown in Fig. 2 due to the transient and reverse transient creep models. In order to evaluate the volumetric non-elastic strain in Eq. (28), we take the trace of Eq. (35), that is,

$$\varepsilon_{ne,v} = \operatorname{tr}(\boldsymbol{\varepsilon}_{ne}) = \underbrace{\operatorname{tr}(\boldsymbol{\varepsilon}^{k}_{ne})}_{\varepsilon^{k}_{ne,v}} + \phi_2 \underbrace{\operatorname{tr}(\mathbb{G}^{k}_{ne} : \delta\boldsymbol{\sigma})}_{\text{Evaluated below}} - \phi_2 \underbrace{\operatorname{tr}(\mathbf{B}^{k}_{ne})}_{B^{k}_{ne,v}}. \tag{36}$$

Using Einstein notation, the middle term in the right-hand side of Eq. (36) can be expanded as

$$\operatorname{tr}(\mathbb{G}^{k}_{ne} : \delta\boldsymbol{\sigma}) = G^{k}_{iikl}\delta\sigma_{kl} = G^{k}_{ii11}\delta\sigma_{11} + G^{k}_{ii22}\delta\sigma_{22} + G^{k}_{ii33}\delta\sigma_{33} + 2G^{k}_{ii12}\delta\sigma_{12} + 2G^{k}_{ii13}\delta\sigma_{13} + 2G^{k}_{ii23}\delta\sigma_{23}, \tag{37}$$

where G_{ijkl} represent the components of the rank-4 tensor $\mathbb{G}_{ne}$. Defining the following rank-2 tensor

$$\mathbf{F}^{k} = \begin{bmatrix} G^{k}_{ii11} & G^{k}_{ii12} & G^{k}_{ii13} \\ G^{k}_{ii12} & G^{k}_{ii22} & G^{k}_{ii23} \\ G^{k}_{ii13} & G^{k}_{ii23} & G^{k}_{ii33} \end{bmatrix}, \tag{38}$$

Eq. (37) can be rewritten as

$$\operatorname{tr}(\mathbb{G}^{k}_{ne} : \delta\boldsymbol{\sigma}) = \mathbf{F}^{k} : \delta\boldsymbol{\sigma}. \tag{39}$$

and the volumetric non-elastic strain can be finally expressed as

$$\varepsilon_{ne,v} = \varepsilon^{k}_{ne,v} + \phi_2 \mathbf{F}^{k} : \delta\boldsymbol{\sigma} - \phi_2 B^{k}_{ne,v}. \tag{40}$$

Substituting Eqs. (35) and (40) into Eq. (28) yields

$$\tilde{\boldsymbol{\varepsilon}}_{ne} = \tilde{\boldsymbol{\varepsilon}}^{k}_{ne} + \phi_2 \left(\tilde{\mathbb{G}}^{k}_{ne} : \delta\boldsymbol{\sigma} - \tilde{\mathbf{B}}^{k}_{ne} \right), \tag{41}$$

where

$$\tilde{\boldsymbol{\varepsilon}}^{k}_{ne} = \boldsymbol{\varepsilon}^{k}_{ne} - \frac{1}{3}\varepsilon^{k}_{ne,v}\mathbf{I}, \tag{42}$$

$$\tilde{\mathbf{B}}^{k}_{ne} = \mathbf{B}^{k}_{ne} - \frac{1}{3}B^{k}_{ne,v}\mathbf{I}, \tag{43}$$

$$\tilde{\mathbb{G}}^{k}_{ne} = \mathbb{G}^{k}_{ne} - \frac{1}{3}\mathbf{I} \otimes \mathbf{F}^{k}. \tag{44}$$

Eq. (41) is now combined with Eqs. (26) and (15) to obtain the linearized stress tensor at step $k+1$. Recalling that

$$\boldsymbol{\sigma} = 2G\left(\tilde{\boldsymbol{\varepsilon}} + \frac{1}{2G} p\mathbf{I} - \tilde{\boldsymbol{\varepsilon}}_{ne} \right), \tag{45}$$

and $\delta\boldsymbol{\sigma} = \boldsymbol{\sigma} - \boldsymbol{\sigma}^{k}$, we have:

$$\left(\frac{1}{2G}\mathbb{I} + \phi_2 \tilde{\mathbb{G}}^{k}_{ne} \right) : \boldsymbol{\sigma} = \tilde{\boldsymbol{\varepsilon}} + \frac{1}{2G} p\mathbf{I} - \tilde{\boldsymbol{\varepsilon}}^{k}_{ne} + \phi_2 \tilde{\mathbb{G}}^{k}_{ne} : \boldsymbol{\sigma}^{k} + \phi_2 \tilde{\mathbf{B}}^{k}_{ne}, \tag{46}$$

with $\mathbb{I}$ denoting the rank-4 identity tensor.

Finally, denoting the rank-4 consistent tangent matrix as

$$\tilde{\mathbb{C}}^{k}_{T} = \left(\frac{1}{2G}\mathbb{I} + \phi_2 \tilde{\mathbb{G}}^{k}_{ne} \right)^{-1}, \tag{47}$$

and grouping together the terms in the right-hand side of Eq. (46) referring to the previous iteration k as

$$\tilde{\boldsymbol{\varepsilon}}^{k}_{\text{rhs}} = \tilde{\boldsymbol{\varepsilon}}^{k}_{ne} - \phi_2 \tilde{\mathbb{G}}^{k}_{ne} : \boldsymbol{\sigma}^{k} - \phi_2 \tilde{\mathbf{B}}^{k}_{ne}, \tag{48}$$

the linearized expression for the stress tensor can be written in a compact form as

$$\boldsymbol{\sigma}(\mathbf{u}, p) = \tilde{\mathbb{C}}^{k}_{T} : \left(\tilde{\boldsymbol{\varepsilon}} + \frac{1}{2G} p\mathbf{I} - \tilde{\boldsymbol{\varepsilon}}^{k}_{\text{rhs}} \right). \tag{49}$$

Eq. (49) is a Newton-like linearization of the stress tensor as a function of the unknowns $\mathbf{u}$ and p. The quantities $\tilde{\mathbb{C}}^{k}_{T}$ and $\tilde{\boldsymbol{\varepsilon}}^{k}_{\text{rhs}}$ are both calculated with information from the previous non-linear iteration k. The presence of the different non-elastic creep elements in Eq. (49) is encoded in the tensors $\tilde{\mathbb{G}}^{k}_{ne}$ and $\tilde{\mathbf{B}}^{k}_{ne}$.

4.2. Linearized momentum balance equation

The linearized momentum balance equation is obtained by substituting Eq. (49) into Eq. (1), which results in

$$\nabla \cdot \tilde{\mathbb{C}}_T^k \,:\, \left[\tilde{\boldsymbol{\varepsilon}}(\mathbf{u}) + \frac{1}{2G} p\, \mathbf{I}\right] = \nabla \cdot \tilde{\mathbb{C}}_T^k \,:\, \tilde{\boldsymbol{\varepsilon}}_{\text{rhs}}^k - \mathbf{b}. \tag{50}$$

Notice that the left-hand side of Eq. (50) carries the unknowns $\mathbf{u}$ and p, while the right-hand side only depends on known quantities.

4.3. Linearized mean stress equation

Since Eq. (50) depends on two unknowns, $\mathbf{u}$ and p, an additional equation is necessary to close the problem. Typically, the mass balance equation is used for this purpose, which, for the case of a solid material, is the mean stress equation, i.e.,

$$K^{-1} p - \varepsilon_{e,v} = 0, \tag{51}$$

where K is the bulk modulus. The elastic volumetric strain relates to the total volumetric strain, the thermal volumetric strain, and the non-elastic volumetric strain by

$$\varepsilon_{e,v} = \varepsilon_v - \varepsilon_{th,v} - \varepsilon_{ne,v}. \tag{52}$$

The volumetric non-elastic strain is the source of non-linearity in Eq. (52), and it is evaluated by the linearized Eq. (40), i.e.,

$$\varepsilon_{e,v} = \varepsilon_v - \varepsilon_{th,v} - \varepsilon_{ne,v}^k - \phi_2 \mathbf{F}^k \,:\, \delta\boldsymbol{\sigma} + \phi_2 B_{ne,v}^k. \tag{53}$$

We note that the stress variation between two non-linear iterations in Eq. (53) can be written as $\delta\boldsymbol{\sigma} = \delta\tilde{\boldsymbol{\sigma}} + \delta p \mathbf{I}$. In this work, we introduce an approximation by assuming the deviatoric stress tensor to be fixed between two consecutive iterations k and $k+1$, that is, $\delta\tilde{\boldsymbol{\sigma}} = 0$. In this way, the non-linear loop becomes an Inexact Newton method as we simply have $\delta\boldsymbol{\sigma} = (p - p^k)\mathbf{I}$ in Eq. (53), which results in

$$\varepsilon_{e,v} = \varepsilon_v - \varepsilon_{th,v} - \varepsilon_{ne,v}^k - \phi_2 \mathbf{F}^k \,:\, \delta p + \phi_2 B_{ne,v}^k. \tag{54}$$

Finally, substituting Eq. (54) into Eq. (51) leads to

$$\left(K^{-1} + \phi_2 F_v^k\right) p - \varepsilon_v = \phi_2 \left(F_v^k p^k + B_{ne,v}^k\right) - \varepsilon_{ne,v}^k - \varepsilon_{th,v}, \tag{55}$$

where $F_v^k = \mathbf{F}^k : \mathbf{I}$. Eq. (55) is the linearized form of the mean stress (or mass) equation. Eqs. (50) and (55) are solved together to obtain the $\mathbf{u}$ and p fields.

5. Weak formulation

In this section, we present the weak forms of the linearized momentum balance, mean stress, and heat diffusion equations. A mixed finite element formulation is proposed for the momentum balance Eq. (1), such that the primary unknowns are displacement ($\mathbf{u}$) and mean stress (p). Moreover, temperature T can be either specified as a constant field in Eq. (1) via creep (i.e., Arrhenius law in Eqs. (18) and (19)), or treated as unknown and determined by solving Eq. (7). Approximations for displacement and temperature fields are obtained by using first-order Sobolev spaces, $H^1(\Omega)$, while the mean stress is sufficient to be defined in $L^2(\Omega)$. We introduce the following continuous trial function spaces

$$\mathcal{U} = \{\mathbf{u} : \Omega \to \mathbb{R}^3 \mid \mathbf{u} \in [H^1(\Omega)]^3, \mathbf{u} = \bar{\mathbf{u}} \text{ on } \Gamma^u\},$$
$$\mathcal{P} = \{p : \Omega \to \mathbb{R} \mid p \in L^2(\Omega)\},$$
$$\mathcal{S} = \{T : \Omega \to \mathbb{R} \mid T \in H^1(\Omega), T = \bar{T} \text{ on } \Gamma^T\},$$

and the corresponding continuous test (weighting) function spaces as

$$\mathcal{U}^0 = \{\mathbf{w} : \Omega \to \mathbb{R}^3 \mid \mathbf{w} \in [H^1(\Omega)]^3, \mathbf{w} = \mathbf{0} \text{ on } \Gamma^u\},$$
$$\mathcal{S}^0 = \{v : \Omega \to \mathbb{R} \mid v \in H^1(\Omega), v = 0 \text{ on } \Gamma^T\}.$$

We emphasize that, since no essential boundary conditions are imposed on the mean stress p, an unconstrained $L^2(\Omega)$ space is sufficient for both the trial and test functions.

5.1. Momentum balance equation

Considering that $\boldsymbol{\sigma} = \boldsymbol{\sigma}(\mathbf{u}, p)$, the standard weak form of Eq. (1) reads

$$\int_\Omega \boldsymbol{\varepsilon}(\mathbf{w}) : \boldsymbol{\sigma}(\mathbf{u}, p) \mathrm{d}\Omega = \int_{\Gamma^\sigma} \mathbf{w} \cdot \bar{\mathbf{t}} \mathrm{d}\Gamma + \int_\Omega \mathbf{w} \cdot \mathbf{b} \mathrm{d}\Omega, \quad \forall\, \mathbf{w} \in \mathcal{U}^0. \tag{56}$$

By introducing the stress linearization (49) into (56), we obtain the incremental weak form of the linear momentum balance:

$$\int_\Omega \boldsymbol{\varepsilon}(\mathbf{w}) : \tilde{\mathbb{C}}_T^k : \left[\tilde{\boldsymbol{\varepsilon}}(\mathbf{u}) + \frac{1}{2G} p \mathbf{I}\right] \mathrm{d}\Omega = \int_{\Gamma^\sigma} \mathbf{w} \cdot \bar{\mathbf{t}} \mathrm{d}\Gamma + \int_\Omega \left[\mathbf{w} \cdot \mathbf{b} + \boldsymbol{\varepsilon}(\mathbf{w}) : \tilde{\mathbb{C}}_T^k : \tilde{\boldsymbol{\varepsilon}}_{\text{rhs}}^k\right] \mathrm{d}\Omega, \quad \forall\, \mathbf{w} \in \mathcal{U}^0. \tag{57}$$

Since the deviatoric strain tensor $\tilde{\boldsymbol{\varepsilon}}(\mathbf{u})$ is expressed as in Eq. (27), the final form of Eq. (57) reads:

$$\int_\Omega \boldsymbol{\varepsilon}(\mathbf{w}) : \tilde{\mathbb{C}}_T^k : \left[\boldsymbol{\varepsilon}(\mathbf{u}) - \frac{1}{3}(\nabla\cdot\mathbf{u})\mathbf{I}\right] \mathrm{d}\Omega + \int_\Omega \boldsymbol{\varepsilon}(\mathbf{w}) : \tilde{\mathbb{C}}_T^k : \left[\frac{1}{2G} p\mathbf{I}\right] \mathrm{d}\Omega = \int_{\Gamma^\sigma} \mathbf{w}\cdot\bar{\mathbf{t}}\,\mathrm{d}\Gamma + \int_\Omega \left[\mathbf{w}\cdot\mathbf{b} + \boldsymbol{\varepsilon}(\mathbf{w}) : \tilde{\mathbb{C}}_T^k : \tilde{\boldsymbol{\varepsilon}}_{\mathrm{rhs}}^k\right] \mathrm{d}\Omega, \quad \forall\ \mathbf{w}\in\mathcal{U}^0. \tag{58}$$

5.2. Mean stress equation

Recalling that $\varepsilon_v = \nabla\cdot\mathbf{u}$, the weak form of Eq. (55) reads

$$\int_\Omega q\left[\left(K^{-1} + \phi_2 F_v^k\right) p\right] \mathrm{d}\Omega - \int_\Omega q\nabla\cdot\mathbf{u}\,\mathrm{d}\Omega = b^k, \quad \forall\ q\in\mathcal{P}. \tag{59}$$

with

$$b^k = \int_\Omega q\left[\phi_2\left(F_v^k p^k + B_{ne,v}^k\right) - \varepsilon_{ne,v}^k - \varepsilon_{th,v}\right] \mathrm{d}\Omega. \tag{60}$$

5.3. Heat diffusion equation

For the prediction of the temperature field required by the constitutive law, the mixed form of the mechanical model is supplemented with the solution of the heat diffusion equation (Eq. (7)) with the related initial and boundary conditions. The standard weak form of Eq. (7) reads

$$\int_\Omega \rho c\frac{\partial T}{\partial t} v\,\mathrm{d}\Omega + \int_\Omega k\nabla T\cdot\nabla v\,\mathrm{d}\Omega + \int_{\Gamma^h} h_{\mathrm{conv}} T v\,\mathrm{d}\Gamma = \int_{\Gamma^h} h_{\mathrm{conv}} T_\infty v\,\mathrm{d}\Gamma - \int_{\Gamma^q} q'' v\,\mathrm{d}\Gamma, \quad \forall\ v\in\mathcal{S}^0. \tag{61}$$

6. Finite element discretization

The solution to Eqs. (58), (59), and (61) is numerically approximated by finite elements. As usual, the domain is divided into discrete elements τ_h, with the solutions $(\mathbf{u}_h, p_h, T_h)$ and the test functions $(\mathbf{w}_h, q_h, v_h)$ belonging to the spaces,

$$\begin{aligned} &\mathbf{u}_h\in\mathcal{U}_h\subset\mathcal{U}, \quad \mathbf{w}_h\in\mathcal{U}_h^0\subset\mathcal{U}^0,\\ &p_h\in\mathcal{P}_h\subset\mathcal{P}, \qquad q_h\in\mathcal{P}_h\subset\mathcal{P},\\ &T_h\in\mathcal{S}_h\subset\mathcal{S}, \qquad v_h\in\mathcal{S}_h^0\subset\mathcal{S}^0. \end{aligned}$$

The finite element spaces are constructed using Continuous Galerkin approximations with piecewise linear basis functions. The use of continuous piecewise linear interpolation for both displacement and mean stress does not, by itself, lead to a stable mixed formulation, since this equal-order pair does not satisfy the inf-sup condition. The choice is nevertheless deliberate, as linear interpolation of the mean stress provides a nonzero intra-element gradient, which is essential for the construction of the stabilization term introduced in Section 7. Thus, the equal-order approximation should be understood as part of the stabilized formulation.

The numerical integration is performed with quadrature rules consistent with the polynomial degree of each term. In particular, one-point quadrature is used for element-wise constant integrands, like strains and stresses, while degree-2 quadrature is adopted for the mass-matrix-like terms appearing in the mean stress and heat equations.

The discrete approximations $(\mathbf{u}_h, p_h, T_h)$ read

$$\mathbf{u}\approx\mathbf{u}_h = \mathbf{u}_h(\mathbf{x},t) = \mathbf{N}_u(\mathbf{x})\hat{\mathbf{u}}(t) \tag{62}$$

$$p\approx p_h = p_h(\mathbf{x},t) = \mathbf{N}_p(\mathbf{x})\hat{p}(t) \tag{63}$$

$$T\approx T_h = T_h(\mathbf{x},t) = \mathbf{N}_T(\mathbf{x})\hat{T}(t) \tag{64}$$

where $\hat{\mathbf{u}}(t)$, $\hat{p}(t)$ and $\hat{T}(t)$ are the vectors of displacements, mean stress and temperature values at the grid nodes at time t, and $\mathbf{N}_u(\mathbf{x})$, $\mathbf{N}_p(\mathbf{x})$ and $\mathbf{N}_T(\mathbf{x})$ are the shape functions defined in $\mathcal{U}_h$, $\mathcal{P}_h$, and $\mathcal{S}_h$, respectively. Notice that $\mathbf{N}_u(\mathbf{x})$ is a matrix rearrangement of $\mathbf{N}_T(\mathbf{x})$ to properly multiply the corresponding displacement components of $\mathbf{u}$. The related gradients are approximated as

$$\boldsymbol{\varepsilon}(\mathbf{u}_h) = \mathbf{B}\hat{\mathbf{u}}, \quad \nabla\cdot\mathbf{u}_h = \mathbf{i}^T\mathbf{B}\hat{\mathbf{u}}, \quad \text{and} \quad \nabla T_h = \mathbf{G}\hat{T},$$

with $\mathbf{i}$ denoting the Kronecker delta column vector, and $\mathbf{G}$ an array of shape function derivatives that recovers the gradient field of a scalar. Similarly, $\mathbf{B}$ is also an array of shape function derivatives to recover the symmetric gradient operator.

6.1. Linear momentum equation

The consistent tangent tensor ($\tilde{\mathbb{C}}_T^k$), defined in Eq. (47), can be represented as a 6×6 matrix using Voigt notation, which we denote as $\tilde{\mathbf{C}}_T^k$. We define the matrices

$$\mathrm{K} = \int_\Omega \left(\mathbf{B}^T \tilde{\mathbf{C}}_T^k \mathbf{B} - \frac{1}{3} \mathbf{B}^T \tilde{\mathbf{C}}_T^k \mathbf{i}\mathbf{i}^T \mathbf{B} \right) \mathrm{d}\Omega, \qquad \mathrm{B}_1 = \int_\Omega \frac{1}{2G} \mathbf{B}^T \tilde{\mathbf{C}}_T^k \mathbf{i} \mathbf{N}_p \mathrm{d}\Omega, \tag{65}$$

$$\mathrm{B}_2 = \int_\Omega \mathbf{N}_p^T \mathbf{i}^T \mathbf{B} \mathrm{d}\Omega, \qquad \mathrm{A} = \int_\Omega \left(K^{-1} + \phi_2 F_v^k \right) \mathbf{N}_p^T \mathbf{N}_p \mathrm{d}\Omega, \tag{66}$$

and the vectors

$$\mathbf{f}_u = \int_{\Gamma^\sigma} \mathbf{N}_u^T \bar{\mathbf{t}} \mathrm{d}\Gamma + \int_\Omega \mathbf{N}_u^T \mathbf{b} \mathrm{d}\Omega + \int_\Omega \mathbf{B}^T \tilde{\mathbf{C}}_T \tilde{\boldsymbol{\varepsilon}}_{\mathrm{vgt}}^k \mathrm{d}\Omega, \tag{67}$$

$$\mathbf{f}_p = \int_\Omega \mathbf{N}_p^T \left[\phi_2 \left(F_v p^k + B_{ne,v}^k \right) - \varepsilon_{ne,v}^k - \varepsilon_{th,v} \right] \mathrm{d}\Omega, \tag{68}$$

where $\tilde{\boldsymbol{\varepsilon}}_{\mathrm{vgt}}^k$ is the Voigt representation of $\tilde{\boldsymbol{\varepsilon}}_{\mathrm{rhs}}^k$. Finally, the linearized system of algebraic equations solved at each iteration of the non-linear loop can be expressed as

$$\begin{bmatrix} \mathrm{K} & \mathrm{B}_1 \\ -\mathrm{B}_2 & \mathrm{A} \end{bmatrix} \begin{bmatrix} \hat{\mathbf{u}} \\ \hat{p} \end{bmatrix} = \begin{bmatrix} \mathbf{f}_u \\ \mathbf{f}_p \end{bmatrix}. \tag{69}$$

6.2. Heat diffusion equation

The weak form of the heat diffusion equation, presented in (61), is integrated in time between t and $t + \Delta t$ by a backward Euler (fully-implicit) scheme, which results in

$$\int_\Omega \left(v \frac{\rho c}{\Delta t} T + k \nabla T \cdot \nabla v \right) \mathrm{d}\Omega + \int_{\Gamma^h} h_{\mathrm{conv}} T v \mathrm{d}\Gamma = \int_\Omega v \frac{\rho c}{\Delta t} T^t \mathrm{d}\Omega + \int_{\Gamma^h} h_{\mathrm{conv}} T_\infty v \mathrm{d}\Gamma - \int_{\Gamma^q} q'' v \mathrm{d}\Gamma, \quad \forall\ v \in \mathcal{S}^0. \tag{70}$$

By defining the quantities

$$\mathrm{M} = \int_\Omega \left(\frac{\rho c}{\Delta t} \mathbf{N}_T^T \mathbf{N}_T + k \mathbf{G}^T \mathbf{G} \right) \mathrm{d}\Omega + \int_{\Gamma^h} h_{\mathrm{conv}} \mathbf{N}_T^T \mathbf{N}_T \mathrm{d}\Omega, \tag{71}$$

$$\mathbf{f}_T = \int_\Omega \frac{\rho c}{\Delta t} \mathbf{N}_T^T \hat{T}^t \mathrm{d}\Omega + \int_{\Gamma^h} h_{\mathrm{conv}} \mathbf{N}_T^T T_\infty \mathrm{d}\Gamma - \int_{\Gamma^q} \mathbf{N}_T^T q'' \mathrm{d}\Gamma, \tag{72}$$

at each time step the temperature field is computed by solving the linear system

$$\mathrm{M} \hat{T} = \mathbf{f}_T. \tag{73}$$

7. Stabilization

Since the finite element spaces used to approximate the displacement and mean stress fields are not an inf-sup stable pair, a stabilization is required to avoid non-physical numerical oscillations of p_h. In this work, we extend the application of the stabilization method developed in [19] for a non-elastic medium.

The idea of Ref. [19] is to enrich the displacement approximation $\mathbf{u}_h$ so as to mimic a higher-order finite element method. This is carried out by noticing that a truncated Taylor expansion of $\mathbf{u}$ in a linear element reads:

$$\mathbf{u} \approx \mathbf{u}_h - h^2 \nabla^2 \mathbf{u}, \tag{74}$$

where h is a geometric parameter that scales the Laplacian of the displacement field. The enrichment of the displacement approximation shown in Eq. (74) requires two different steps: (i) the calculation of the parameter h and (ii) the approximation of the Laplacian of $\mathbf{u}$. The procedure used to estimate h has been developed and described in detail in [19], so here we provide only a brief discussion. By distinction, the approximation of the Laplacian term in Eq. (74) is a major issue for stabilization in the presence of creep and will be described in detail in this section.

7.1. Parameter h

It can be shown that the parameter h can be exactly computed for a regularly shaped hexahedron. However, an analytical expression for h is not available for general elements. In the literature, this parameter has often been regarded as a characteristic measure of the size of the element where the expansion is performed. Common calculations consist of taking the radius of an inscribed sphere, or the diagonal of a cube with the same volume as the element. An alternative interpretation is proposed in [19], where h is calculated in such a way to optimize the representation by Eq. (74) of a general polynomial function at the integration point of a tetrahedron. This optimization process is rather expensive, so a machine learning approach was proposed to speed-up computations. For this purpose, the (expensive) optimization problem was solved to determine h for many different tetrahedral

elements with different sizes and orientations. We carried out this process for approximately 30 thousand elements and used these data to train a machine learning model that predicts the value of h for any set of vertex coordinates of a tetrahedron. We calculate the parameters h for the meshes in the present work using this pre-trained machine learning model. The reader is referred to [19] for further details.

7.2. Laplacian approximation

The approximation of the Laplacian of the displacement, $\nabla^2\mathbf{u}$, is achieved through the Physical Influence Scheme (PIS). This method relies on evaluating the momentum balance equation in a single tetrahedral element, where all material properties are constants. Using the stress split presented in Eq. (15) and neglecting body forces, the momentum balance equation reads

$$\nabla \cdot (\tilde{\boldsymbol{\sigma}} + p\mathbf{I}) = 0. \tag{75}$$

In this work, we consider two different approaches to evaluate Eq. (75) within an element and obtain an approximation of $\nabla^2\mathbf{u}$.

7.2.1. Approach 1: stab−E

From Eq. (26), and recalling that the material properties are constant inside each element, Eq. (75) becomes

$$\nabla \cdot \tilde{\boldsymbol{\varepsilon}} = \nabla \cdot \tilde{\boldsymbol{\varepsilon}}_{ne} - \frac{1}{2G}\nabla p. \tag{76}$$

If we neglect the term $\nabla \cdot \tilde{\boldsymbol{\varepsilon}}_{ne}$, for example assuming that the non-elastic strain is constant inside the element, we can write

$$\nabla \cdot \left(\boldsymbol{\varepsilon} - \frac{1}{3}\varepsilon_v \mathbf{I}\right) \approx -\frac{1}{2G}\nabla p. \tag{77}$$

where $\tilde{\boldsymbol{\varepsilon}}$ has been expressed by using Eq. (27). After recognizing that $2\nabla \cdot \boldsymbol{\varepsilon} = \nabla^2\mathbf{u} + \nabla\varepsilon_v$ and $\varepsilon_v = \varepsilon_{ne,v} + \frac{1}{K}p$, the following expression is obtained,

$$\nabla^2\mathbf{u} \approx -\left(\frac{1}{3K} + \frac{1}{G}\right)\nabla p - \frac{1}{3}\nabla\varepsilon_{ne,v}. \tag{78}$$

The assumption on constant non-elastic strain also yields $\nabla\varepsilon_{ne,v} = 0$. Therefore, we can conclude that the Laplacian of displacement is approximately proportional to the mean stress gradient, that is,

$$\nabla^2\mathbf{u} \approx -\frac{3}{E}\nabla p. \tag{79}$$

with E denoting Young's modulus. Substituting (79) into Eq. (74) yields

$$\mathbf{u} \approx \mathbf{u}_h + h^2\frac{3}{E}\nabla p. \tag{80}$$

Notice that the approximation in Eq. (79) in the end completely disregards non-elastic strains. While this can be acceptable in the beginning of the simulation, the approximation can become too rough as non-elastic strains accumulate with time.

7.2.2. Approach 2: stab−E*

In order to account for non-elastic deformations in the Laplacian approximation, we adopt a similar concept as introduced in [22]. It consists of transferring the effect of non-elastic strains to a modification of the shear modulus, as if the material becomes weaker. In this manner, the total strain is regarded elastic, whereas the elastic property (shear modulus) is updated accordingly. Hence, Eq. (26) reads

$$\tilde{\boldsymbol{\sigma}} = 2G\left(\tilde{\boldsymbol{\varepsilon}} - \tilde{\boldsymbol{\varepsilon}}_{ne}\right) \approx 2G^*\tilde{\boldsymbol{\varepsilon}}, \tag{81}$$

where G^* is referred to as the *secant* shear modulus [22]. Using Eq. (81), the effect of the non-elastic strains is lumped into the calculation of G^*, so they are not ignored.

Substituting (81) into (75) provides

$$\nabla \cdot \tilde{\boldsymbol{\varepsilon}} \approx -\frac{1}{2G^*}\nabla p. \tag{82}$$

and again, recalling Eq. (27) and that $2\nabla \cdot \boldsymbol{\varepsilon} = \nabla^2\mathbf{u} + \nabla\varepsilon_v$, it follows that

$$\nabla^2\mathbf{u} \approx -\frac{1}{3}\nabla\varepsilon_v - \frac{1}{G^*}\nabla p. \tag{83}$$

Similarly to the secant shear modulus, the effect of non-elastic volumetric strains can be lumped into a *secant* bulk modulus, K^*, as follows,

$$p = K\left(\varepsilon_v - \varepsilon_{ne,v}\right) \approx K^*\varepsilon_v \quad \rightarrow \quad \varepsilon_v \approx \frac{p}{K^*}. \tag{84}$$

Finally, substituting (84) into Eq. (83) leads to

$$\nabla^2\mathbf{u} \approx -\left(\frac{1}{3K^*} + \frac{1}{G^*}\right)\nabla p = -\frac{3}{E^*}\nabla p, \tag{85}$$

and the truncated Taylor expansion of the displacement can be written as

$$\mathbf{u} \approx \mathbf{u}_h + h^2 \frac{3}{E^*} \nabla p. \tag{86}$$

By extension of terminology, E^* is referred to as the *secant* Young's modulus. In this work, the calculation of E^* is performed based on the principal stresses and the principal total strains, that is,

$$E^* = \frac{\sigma_1 - \nu\left(\sigma_2 + \sigma_3\right)}{\varepsilon_1}, \tag{87}$$

where $\sigma_1 > \sigma_2 > \sigma_3$ and $\varepsilon_1 > \varepsilon_2 > \varepsilon_3$. The values of E^* are calculated at each integration point based on stress and strain values taken from the previous non-linear iteration k.

Note that if the material is purely elastic, Eq. (87) produces the elastic Young's modulus E. Otherwise, if a larger deformation ε_1 is obtained for the same principal stresses, we obtain $E^* < E$. In other words, the material appears to be weaker because of the presence of non-elastic strains. As a consequence, $3/E^*$ increases in Eq. (86) as the non-elastic strains accumulate, thus growing the effect of the stabilization terms for elements of the mesh where creep is developing more.

7.3. Stabilized discrete equations

Eq. (80) or (86) is introduced in the continuous weak form of the mean stress Eq. (59), with p replaced by its finite element approximation p_h. The resulting discrete weak form reads

$$\int_\Omega q_h \left[\left(K^{-1} + \phi_2 F_v^k\right) p_h\right] \mathrm{d}\Omega - \int_\Omega q_h \nabla \cdot \left(\mathbf{u}_h + h^2 \frac{3}{E_{\text{stab}}} \nabla p_h\right) \mathrm{d}\Omega = b_h^k, \quad \forall\ q_h \in \mathcal{P}_h, \tag{88}$$

where

$$b_h^k = \int_\Omega q_h \left[\phi_2 \left(F_v^k p_h^k + B_{ne,v}^k\right) - \varepsilon_{ne,v}^k - \varepsilon_{th,v}\right] \mathrm{d}\Omega,$$

and E_{stab} is either E or E^* if the stab$-E$ or stab$-E^*$ approach is chosen. Then, we use integration by parts to evaluate the rightmost term inside the integral. Notice that the boundary term does not appear because the stabilization corresponds to a homogeneous Neumann problem for the Laplace equation on p. After this procedure, the following equation is obtained

$$\int_\Omega q_h \left[\left(K^{-1} + \phi_2 F_v^k\right) p_h\right] \mathrm{d}\Omega + \int_\Omega h^2 \frac{3}{E_{\text{stab}}} \nabla q_h \cdot \nabla p_h \mathrm{d}\Omega - \int_\Omega q_h \nabla \cdot \mathbf{u}_u \mathrm{d}\Omega = b_h^k, \quad \forall\ q_h \in \mathcal{P}_h. \tag{89}$$

While in the unstabilized formulation the gradient of p does not appear, the weak form (89) contains ∇p_h and ∇q_h. Therefore, in the stabilized formulation, both the trial and test functions must belong to $H^1(\Omega)$, with the corresponding space $\mathcal{P}_h$ subspace of

$$\mathcal{P} = \{p : \Omega \to \mathbb{R} \mid p \in H^1(\Omega)\}. \tag{90}$$

Since no essential boundary conditions are applied to p, the trial and test spaces coincide.

Finally, introducing the discrete approximations $\mathbf{u}_h$, p_h, and q_h into Eq. (89) leads to the linearized form of the stabilized discrete equations. Since now $\mathcal{P}_h$ has the same requirements as S_h^0, we can set $\mathbf{N}_p(\mathbf{x}) = \mathbf{N}_T(\mathbf{x})$, obtaining:

$$\begin{bmatrix} \mathrm{K} & \mathrm{B}_1 \\ -\mathrm{B}_2 & \mathrm{A} + \mathrm{H} \end{bmatrix} \begin{bmatrix} \hat{\mathbf{u}} \\ \hat{p} \end{bmatrix} = \begin{bmatrix} \mathbf{f}_u \\ \mathbf{f}_p \end{bmatrix}, \tag{91}$$

where

$$\mathrm{H} = \int_\Omega h^2 \frac{3}{E_{\text{stab}}} \mathbf{G}^T \mathbf{G} \mathrm{d}\Omega. \tag{92}$$

It is worth to emphasize that, although the corrected displacement approximation acts as a higher-order enrichment, the resulting stabilized formulation still preserves second-order convergence for both displacement and mean stress. Evidence supporting this behavior was provided in [16] for a mathematically analogous coupled poroelasticity problem, in which displacement and pore pressure were the primary variables. In that work, the same Physical Influence Scheme (PIS) was employed to enrich the displacement field in a manner analogous to that adopted here, and the corresponding convergence study demonstrated that the discrete stabilized formulation is consistent for $h \to 0$ and retained second-order accuracy.

8. Results

The test cases presented in this section are meant to investigate different aspects of the proposed stabilized mixed formulation. The first test case is employed to verify that the mixed formulation ($\mathbf{u} - p$) produces similar results as the primal ($\mathbf{u}$) one in an oscillation-free condition. The remaining test cases assess the stabilization scheme in different scenarios, considering constitutive models that produce zero and non-zero spherical non-elastic strains. The material parameters used in all test cases are summarized in Table 1. The specific combinations of elements for the constitutive models are specified in each test case.

Table 1
Material properties used in test cases 1, 2, 3, and 4 [28,30].

Element	Symbol	Unit	Value
Elastic	E	GPa	102
	ν	–	0.3
Dislocation creep	A_{ds}	$Pa^{-n}\ s^{-1}$	1.1×10^{-21}
	n	–	3.0
	Q_{ds}	J/mol	51 600
Pressure solution creep	A_{ps}	$Pa^{-n}\ s^{-1}$	1.29×10^{-19}
	Q_{ps}	J/mol	72 819
	d	mm	10
Kelvin-Voigt (viscoelastic)	E	GPa	10
	ν	–	0.32
	η	GPa s	1.05×10^{13}
Viscoplastic	μ_1	s^{-1}	5.37×10^{-11}
	N_1	–	3.1
	n_1	–	3.0
	a_1	MPa^{n-2}	1.96×10^{-5}
	η	–	0.827
	β_1	MPa^{-1}	0.0048
	β	–	0.995
	m	–	−0.5
	γ	–	0.095
	σ_t	MPa	5.0
Thermoelastic	α_{th}	K^{-1}	1×10^{-5}

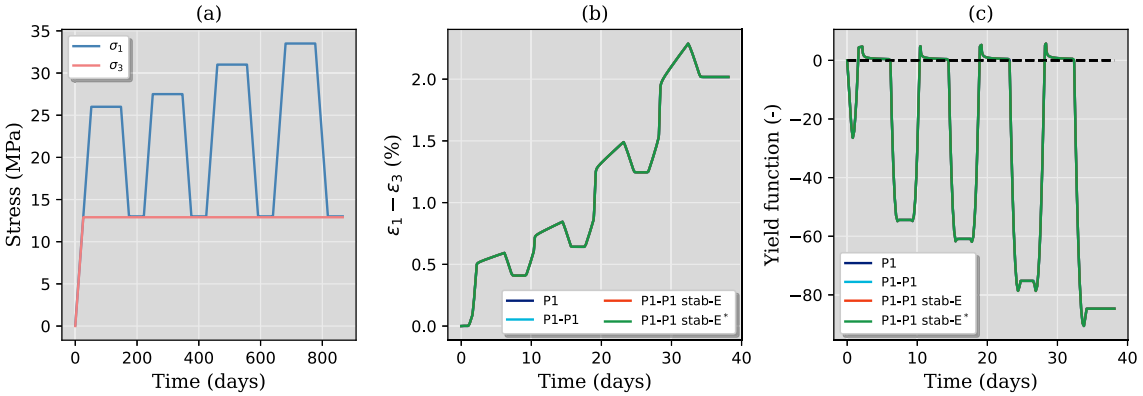

Fig. 3. (a) Stresses imposed as boundary conditions, (b) resulting differential strains, and (c) yield function values.

8.1. Test case 1: Triaxial load

The main goal in this test case is to show that all the formulations (i.e., P1, P1-P1, P1-P1 stab-E, and P1-P1 stab-E*) produce the same results in the absence of spurious oscillations. This situation is obtained in a triaxial test, where the stresses applied on the boundaries are the same perceived by every mesh cell. For this case, we consider a $1 \times 1 \times 1$ m^3 cube with faces *West* ($x = 0$), *South* ($y = 0$), and *Bottom* ($z = 0$) prevented from normal displacement; boundaries *East* ($x = 1$ m) and *North* ($y = 1$ m) subjected to the compressive stress σ_3 shown in Fig. 3-a; and σ_1 imposed on boundary *Top* ($z = 1$ m) also according to Fig. 3-a. The constitutive model for this test case considers elastic, transient creep (viscoplastic), dislocation creep, pressure-solution creep, and reverse transient creep (viscoelastic).

Since the resulting stress field is the same for every cell in the grid, so is the strain field. In this manner, we monitor the differential stress field ($\varepsilon_1 - \varepsilon_3$) in a certain grid cell over time, and the results are shown in Fig. 3-b. The yield function values (Eq. (21)) are also plotted over time and presented in Fig. 3-c. As can be verified, all formulations produce the same results as expected.

8.2. Test case 2: Plate with circular hole

This test case consists of solving the plate with circular hole problem, whose geometry and boundary conditions are depicted in Fig. 4-a. The mesh is composed of tetrahedral elements with a refinement in the near-hole region. The problem was originally proposed for a linear elastic material, for which an analytical solution of the stress field is available [31]. In the present work,

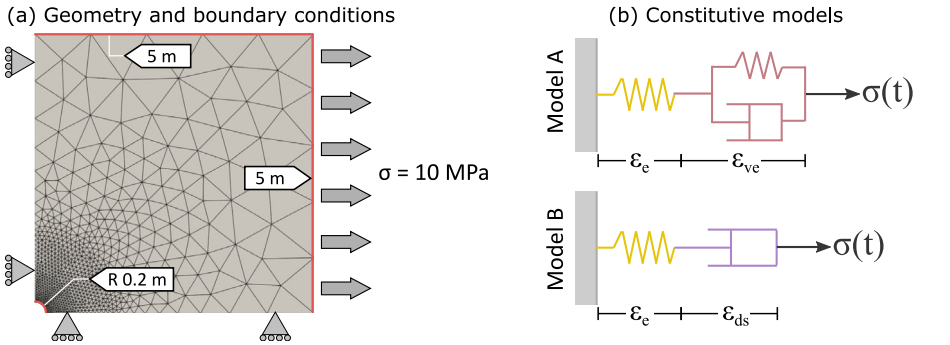

Fig. 4. (a) Geometry dimensions and boundary conditions for the Test Case 2 and (b) constitutive models.

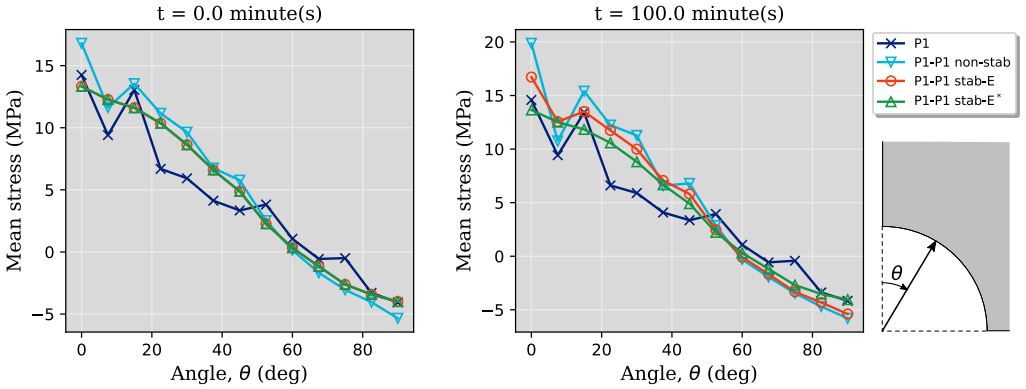

Fig. 5. Plate with circular hole: mean stress profiles along the circular hole obtained with Model A (viscoelastic).

however, we consider two different material models, as depicted in Fig. 4-b. Model A is known as the Voigt form of the Standard Linear Solid model. This model allows for viscoelastic volumetric deformations to take place, since the full stress tensor (i.e., deviatoric plus spherical parts) is present in the viscoelastic strain rate expression (see Eq. (17)). Model B, on the other hand, is the classical Maxwell's model equipped with the power law creep model described by Eq. (18), in which inelastic volumetric deformations are not allowed. In summary, all components of tensor $\mathbf{F}^k$ in Eq. (38) are zero for Model B, but not for Model A. The same holds for F_v^k in the mean stress equation. In this way, we are able to evaluate the formulation under two extreme situations. Finally, since both models are time dependent, a transient simulation is performed. For Model A, the final time is 0.1 day with a time step size of 0.001 day. For Model B, the final time is 100 days with a time step size of 2 days.

For Model A, the mean stress profiles are plotted along the internal faces of the circular hole for the initial and final time steps, as shown in Fig. 5. The results show that the primal P1 formulation produces considerable oscillations since the beginning of the simulation. The mixed P1-P1 formulation is less oscillatory, but oscillations are also present since the first time step. By adding the stabilization terms *stab-E*, the oscillations are initially suppressed but eventually appear in the results, as the secant Young's modulus E^* starts to differ significantly from the elastic one E. By introducing the *stab-E** method, no oscillations have been observed during the transient simulation. The three-dimensional oscillatory pattern of these numerical solutions can be observed in Fig. 6 for the final simulation time. Despite the results in Fig. 5, oscillations can be hardly observed for the E−stabilized P1-P1 formulation in Fig. 6-c. In agreement with Fig. 5, the results shown in Fig. 6 are also smooth.

The same type of results are shown in Figs. 7 and 8 for Maxwell's model (i.e., Model B). The solutions at $t = 0.0$ are the same for both Models A and B because this is the elastic response of the material. For the final time ($t = 90$ days), however, the primal P1 solution is extremely oscillatory, which can also be observed in Fig. 8-a. Once again, the stabilization *stab-E* produces less oscillations than the non-stabilized mixed formulation, but is still oscillatory by the end of the simulation. On the other hand, the E^*−stabilized mixed P1-P1 formulation exhibits no oscillations throughout the full transient solution. This is also confirmed in Fig. 8, which shows a completely smooth mean stress field for the E^*−stabilization, whereas oscillatory patterns are obtained with the other formulations.

8.3. Test case 3: Salt cavern with viscoplastic model

In this problem, we simulate a hydrogen ($\rho = 0.082$ kg/m^3) storage operation in a salt cavern. The geometry and boundary conditions are shown in Fig. 9-a and -b, respectively. The entire domain is considered as a salt layer ($\rho = 2000$ kg/m^3), which is

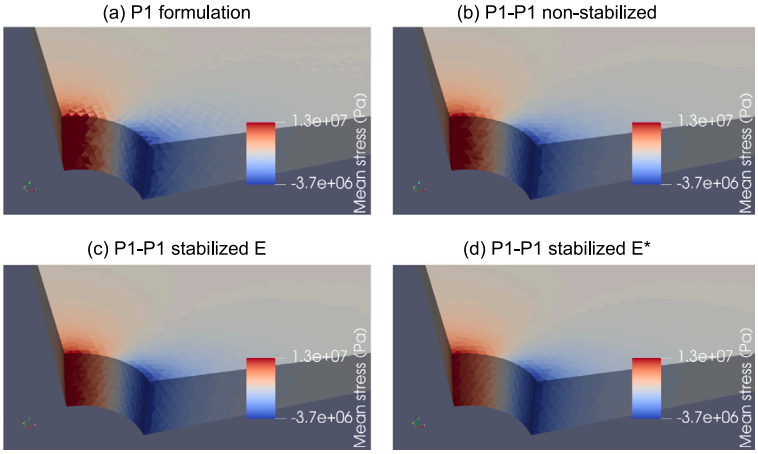

Fig. 6. Plate with circular hole: Mean stress fields obtained with Model A (viscoelastic).

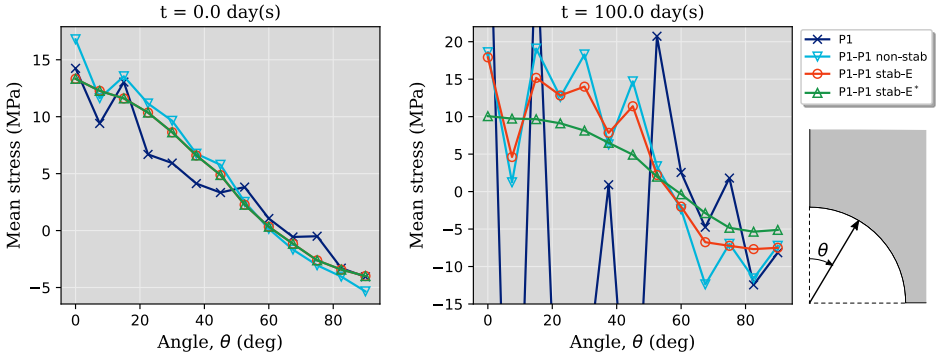

Fig. 7. Plate with circular hole: mean stress profiles along the circular hole obtained with Model B (dislocation creep).

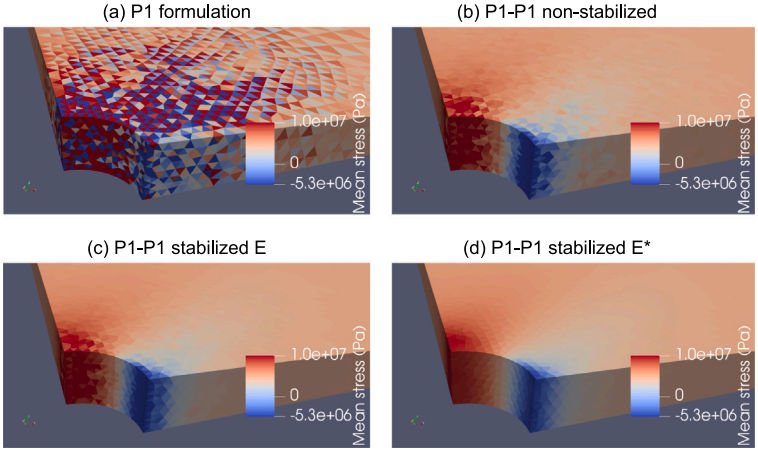

Fig. 8. Plate with circular hole: Mean stress fields obtained with Model B (dislocation creep).

subjected to a 10 MPa overburden and a sideburden following the specific weight of salt, as indicated in Fig. 9-b. The simulation is divided in two stages. The first one is referred to as *equilibrium* stage, and its purpose is to calculate the initial stresses for the actual *operation* (storage) stage. As depicted in Fig. 9-c, the gas pressure is kept constant during the equilibrium stage and equal to 10 MPa at the top of the cavern, and it increases with depth according to hydrogen's specific weight. The equilibrium stage is run for 100 days with a time step size of 2 days. Moreover, the viscoplastic element in the constitutive model illustrated in Fig. 9-d is excluded from the equilibrium stage, as it does not affect the final stress condition. When the equilibrium condition is achieved, the

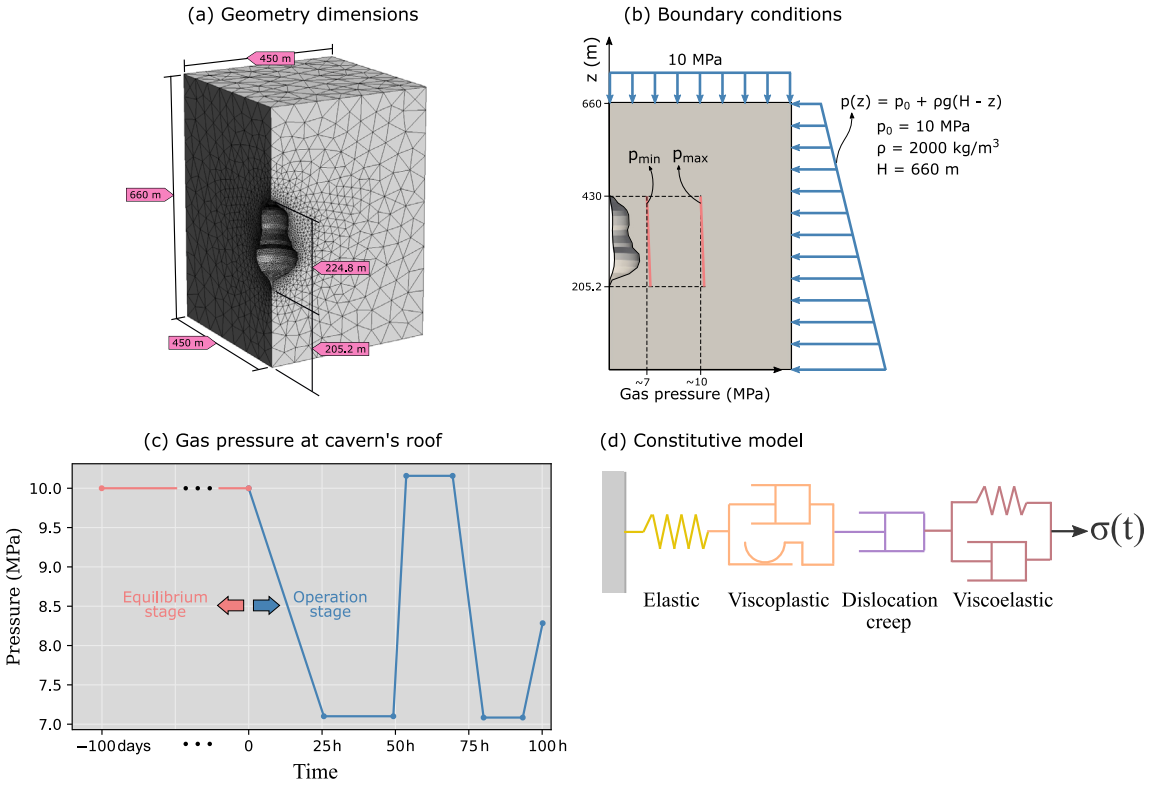

Fig. 9. Geometry, boundary conditions, gas pressure history and constitutive model for test case 3. (For interpretation of the references to color in this figure legend, the reader is referred to the web version of this article.)

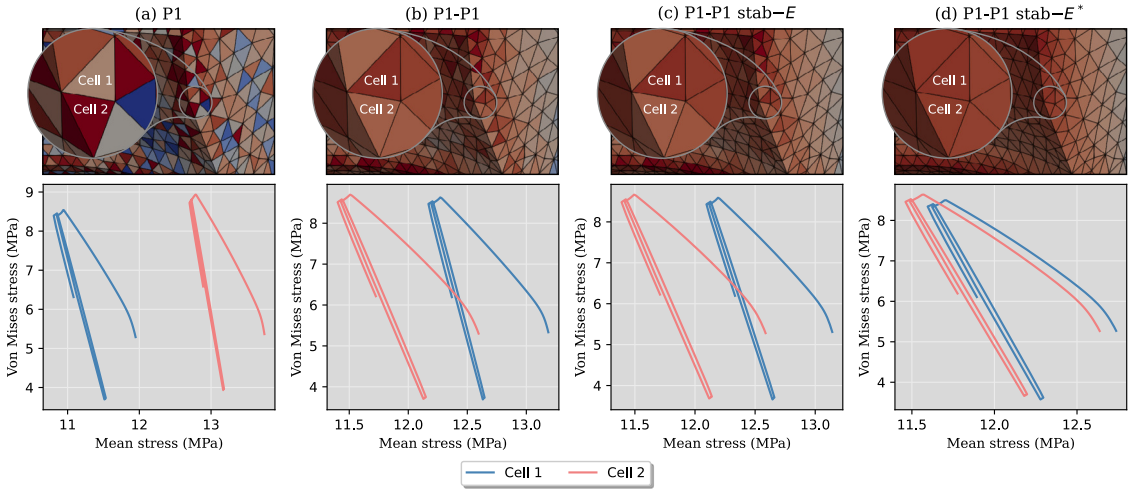

Fig. 10. Stress paths at two adjacent cells (Cell 1 and 2) obtained with the four formulations.

resulting stress field is used to calculate the initial hardening parameter according to Eq. (24), such that every grid element is in the onset of viscoplastic deformation (i.e., $F^*_{vp} = 0$). Therefore, the full constitutive model shown in Fig. 9-d is used in the operation stage, and gas pressure at the cavern's roof follows the blue curve indicated in Fig. 9-c. The operation stage is run for 100 h with an adaptive time step size varying between 0.5 to 5.0 h depending on the maximum yield function (F_{vp}) value in the domain.

The stress paths obtained with formulations P1, P1-P1, P1-P1 stab−E, and P1-P1 stab−E^* are shown in Fig. 10. The graphs show the stress paths for two adjacent cells, named *Cell 1* and *Cell 2*. The mesh is sufficiently refined such that the stresses are not expected to vary abruptly between neighboring cells. Nevertheless, the graphs in Fig. 10-a show very different stress paths for cells 1 and

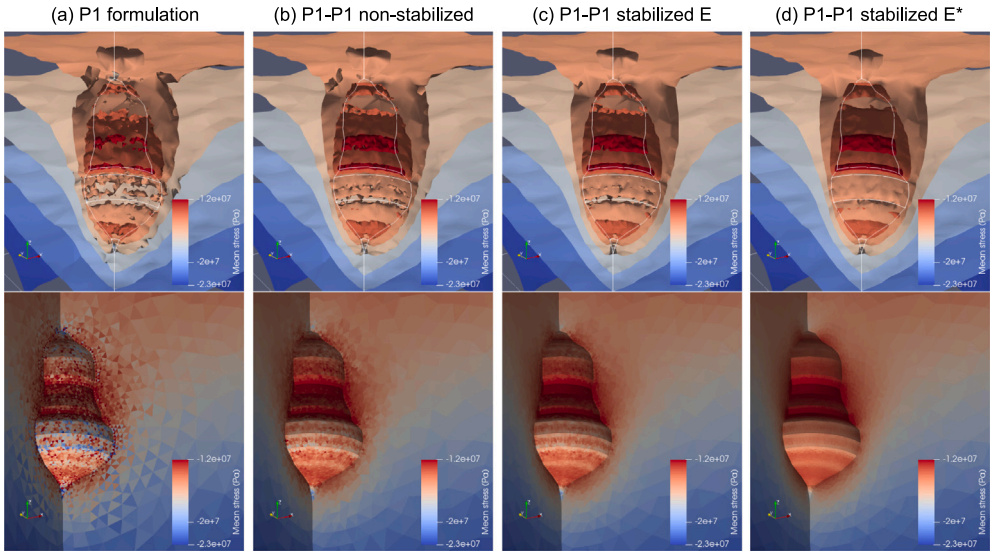

Fig. 11. Test case 3: mean stress results for the cavern at $t = 100$ h.

2 obtained with the primal P1 formulation. Fig. 10-b and -c reveal that the non-stabilized and stab$-E$ mixed P1-P1 formulations reduces the stress variations between the two cells, but the outcome suggests that these are still a product of oscillatory patterns. In contrast, the mean stress field obtained with the mixed P1-P1 stab$-E^*$ is completely smooth, which is reflected in a small variation between the stress paths in the two neighboring cells. The superiority of the mixed P1-P1 stab$-E^*$ formulation is also confirmed in Fig. 11, where the mean stress isosurfaces (top row) and fields (bottom row) are shown for the end of the simulation.

8.4. Test case 4: Salt cavern with thermal effects

In this numerical experiment, we simulate the thermomechanical behavior of a salt cavern considering an elastic overburden and a salt layer, as shown in Fig. 12-a. The constitutive model used for the salt rock is depicted in Fig. 12-b, where dislocation creep, pressure solution creep, reverse transient creep (viscoelastic element), and thermal strains are considered. The heat diffusion equation is also solved to compute the temperature distribution at each time step. The initial temperature distribution is also shown in Fig. 12-a. Temperature is prescribed on the surface, heat flux is imposed on the bottom boundary compatible with the geothermal gradient, convective heat transfer ($h_{\text{conv}} = 5$ W/m^2/K and $T_\infty = T_{\text{gas}}(t)$ shown in Fig. 12-c) is imposed on the cavern walls, and all the remaining boundaries are isolated. For momentum balance equations, zero normal displacements are imposed on all boundaries, except for the top surface, which is stress free, and the cavern walls, which are subjected to the gas pressure shown in Fig. 12-d. A purely mechanical (i.e., no thermal strains and no heat transfer) equilibrium stage is solved at constant pressure for 20 days to calculate the initial stress conditions.

This test case is simulated using the four investigated formulations (i.e., primal P1, mixed P1-P1 without stabilization, mixed P1-P1 stab-E and stab-E^*). Fig. 13-a compares the means stress results over time at a certain point around the cavern. It can be verified that the P1 formulation results in large mean stress variations (amplitudes) in an overall descending trend. The non-stabilized and E-stabilized mixed formulations provide similar results and do not show the descending trend. Finally, the E^*-stabilized mixed formulation results in a significantly smaller amplitude. In terms of von Mises stress, shown in Fig. 13-b, the P1-P1 stab E^* produces a very different result when gas pressure is at high plateaus. Lastly, the volume of the cavern is monitored over time and plotted in Fig. 13-c. All the mixed formulations produce similar results, but the primal P1 formulation significantly underestimate the storage volume loss due to creep.

Fig. 13 indicate two specific instants where gas pressure is at high and low values. These, of course, produce very different stress responses, which are shown in Figs. 14 and 15 for high and low gas pressure, respectively. As shown in Fig. 14-a, the primal P1 formulation produces a highly oscillatory mean stress field, as expected, but also the von Mises stress field shows oscillatory patterns. Although smaller, mean stress and von Mises stress spurious oscillations are also observed for the non-stabilized and stab-E mixed formulations (Fig. 14-b and -c). Conversely, Fig. 14-d shows that the P1-P1 stab-E^* formulation produces fairly smooth stress fields.

During low gas pressure cycles, the loads are transferred to the cavern walls, thus producing higher stresses. Fig. 15 shows the stresses around the cavern for $t = 60$ days. In this case, the obtained von Mises stresses are very similar to each other, with the primal P1 resulting in slightly smaller values. This causes slower creep rates that justify the volume loss underestimation shown in Fig. 13-c. After 60 h, the amount of inelastic strain accumulated in the rock mass, especially near the cavern, practically invalidates the assumption of negligible $\nabla \cdot \tilde{\boldsymbol{\varepsilon}}_{ne}$ and $\nabla \varepsilon_{ne,v}$ contributions in the P1-P1 stab-E formulation, causing its solution to be very close to the non-stabilized P1-P1 formulation. Once again, the mean stress solution for the mean stress field obtained with the P1-P1 stab-E^* approach is completely smooth, as the stabilization parameters locally adapt according to the level of the non-elastic strain.

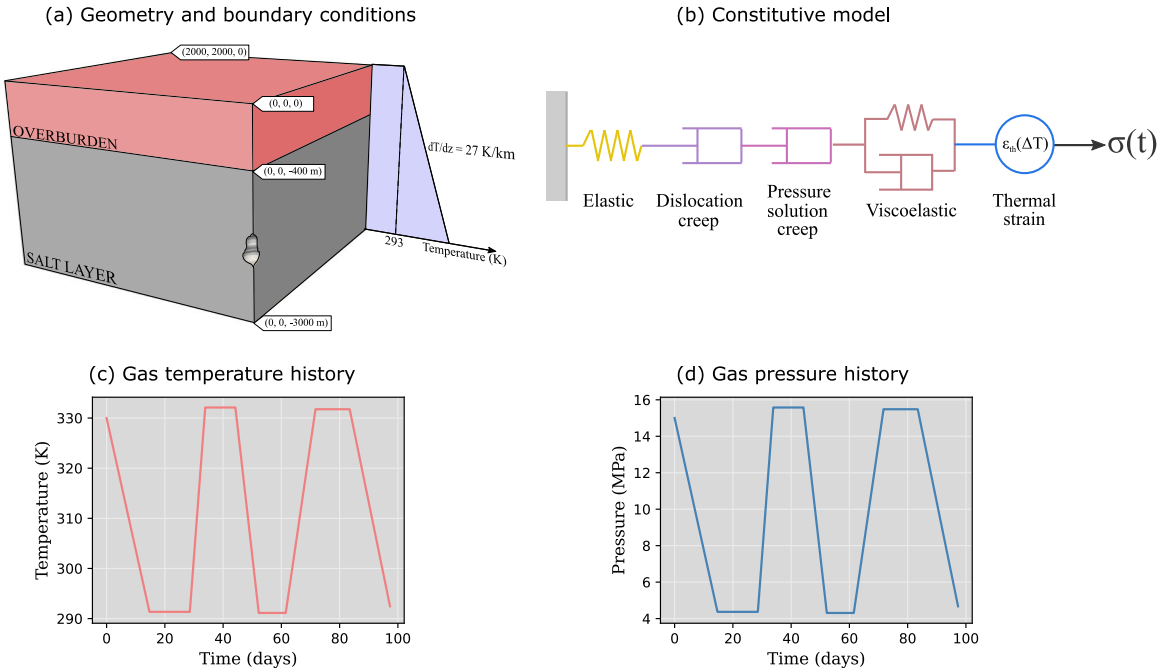

Fig. 12. Operation stage: Mean stress fields obtained with the Mixed FE formulation with different values of β at $t = 100$ h.

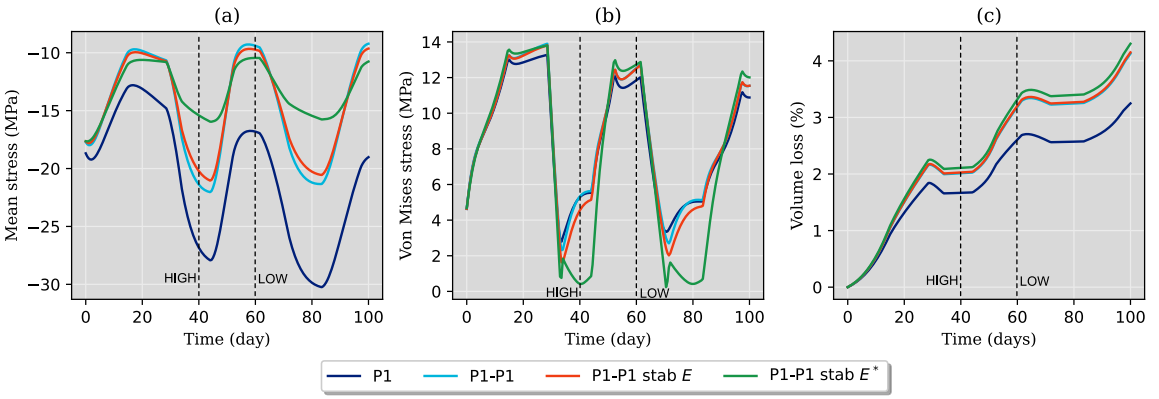

Fig. 13. Time variation of (a) mean stress, (b) von Mises stress, (c) and volumetric loss of the cavern.

9. Conclusions

This paper presented a stabilized mixed finite element formulation for the simulation of salt caverns with tetrahedral meshes. The mixed formulation consists of isolating the mean stress field from the stress tensor, and solving for displacement and mean stress using linear interpolations (P1-P1). Stabilization terms are introduced into the mean stress equation by properly enriching the displacement field in a physically consistent way (PIS). Additionally, the concept of secant Young's modulus has been introduced, which promotes localized stabilization in critical regions and was shown to be crucial in eliminating spurious oscillations as creep develops. Moreover, the proposed formulation does not require any type of user-defined tuning parameters, and is able to produce physically consistent results regardless of the deformation types. The constitutive model considered in this work comprises transient and reverse transient creep, steady-state creep (both pressure-solution and dislocation mechanisms), and thermal strains. These deformation mechanisms have been systematically tested within the proposed formulation and no spurious oscillations have been observed.

The main motivation for this work is to avoid the use of hexahedral meshes for the discretization of salt caverns. Hexahedral elements are known to be more accurate, and locking could be readily alleviated, for instance, by means of the B-bar method. However, generating hexahedral meshes for cavern systems with complex shapes can be highly time-consuming. This is precisely the context in which tetrahedral meshes are most attractive, as they are considerably easier to generate and to locally refine. The

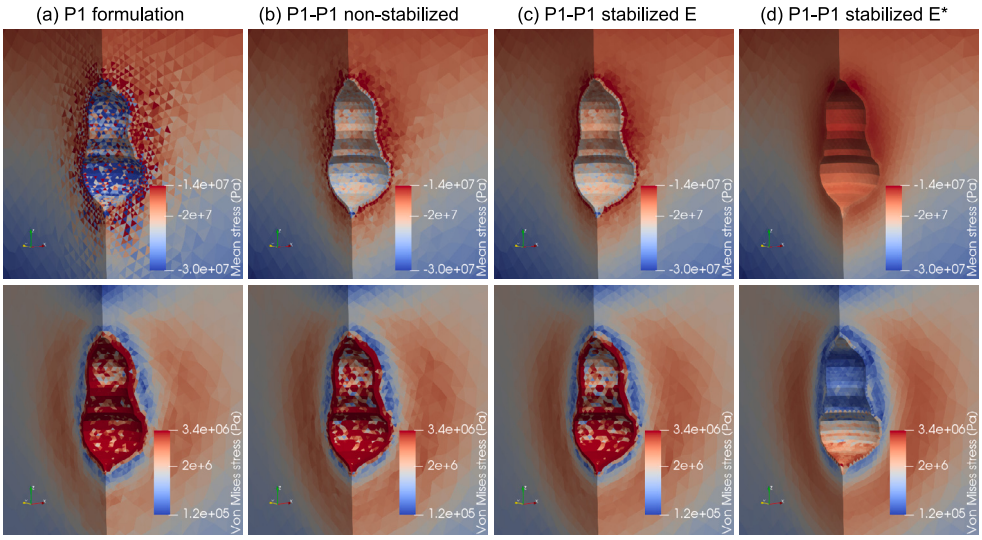

Fig. 14. Mean stress (first row) and von Mises stress (second row) fields for all formulations taken at high cavern pressure ($t = 40$ days, as shown in Fig. 13).

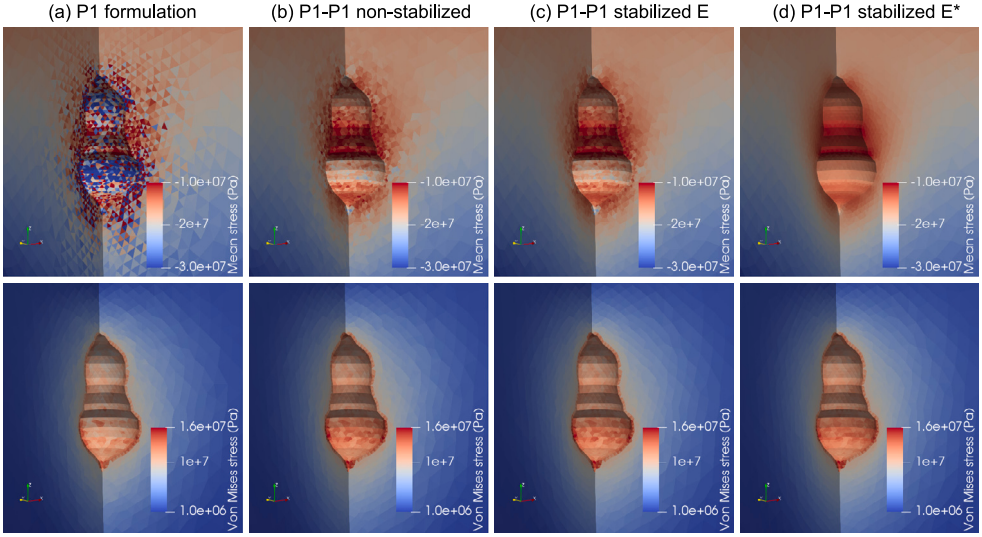

Fig. 15. Mean stress (first row) and von Mises stress (second row) fields for all formulations taken at low cavern pressure ($t = 80$ days, as shown in Fig. 13).

trade-off is the need to deal with locking, that is, spurious oscillation phenomena, which makes the numerical formulation more complex to develop and implement. Ultimately, one must decide where to concentrate effort: on mesh generation or on the numerical scheme. The present work chooses the latter, based on the view that implementing a robust numerical formulation for tetrahedral meshes is a one-time investment that pays off whenever a new complex geometry must be discretized. An important next step, therefore, is to apply the proposed formulation to realistic cavern configurations with intricate geometries, so that its practical potential in truly application-driven settings can be fully assessed.

CRediT authorship contribution statement

Hermínio T. Honório: Writing – original draft, Visualization, Validation, Software, Methodology, Formal analysis, Conceptualization. **Andrea Franceschini:** Writing – review & editing, Methodology, Formal analysis, Conceptualization. **Massimiliano Ferronato:** Writing – review & editing, Methodology, Conceptualization. **Hadi Hajibeygi:** Writing – review & editing, Supervision, Methodology, Funding acquisition, Conceptualization.

Declaration of competing interest

The authors declare that they have no known competing financial interests or personal relationships that could have appeared to influence the work reported in this paper.

Acknowledgments

This research was mainly supported by the Energi Simulation Chair in Subsurface Storage and Multiscale Modeling. H.T.H was also supported by TNO-GDN. A.F. and M.F. are members of Gruppo Nazionale Calcolo Scientifico - Istituto Nazionale di Alta Matematica (GNCS-INdAM). The authors acknowledge members of the ADMIRE and DARSim research groups at TU Delft for fruitful discussions during the development of this work.

Data availability

The source code and all the scripts used generate the results presented in this paper are publicly available in our GitHub repository.

References

[1] K. Ramesh Kumar, A. Makhmutov, C.J. Spiers, H. Hajibeygi, Geomechanical simulation of energy storage in salt formations, Sci. Rep. 11 (1) (2021/10/04) 19640, http://dx.doi.org/10.1038/s41598-021-99161-8.
[2] P. Bérest, B. Brouard, Safety of salt caverns used for underground storage: Blow out; mechanical instability; seepage; cavern abandonment, Oil & Gas Sci. Technol. – Rev. D'IFP Energies Nouv. 58 (3) (2003) 361–384, http://dx.doi.org/10.2516/ogst:2003023.
[3] K. Khaledi, E. Mahmoudi, M. Datcheva, T. Schanz, Stability and serviceability of underground energy storage caverns in rock salt subjected to mechanical cyclic loading, Int. J. Rock Mech. Min. Sci. 86 (2016) 115–131, http://dx.doi.org/10.1016/j.ijrmms.2016.04.010.
[4] F. Brezzi, M. Fortin, Mixed and Hybrid Finite Element Methods, Vol. 15, Springer Science & Business Media, 2012.
[5] T.J. Hughes, L.P. Franca, M. Balestra, A new finite element formulation for computational fluid dynamics: V. circumventing the Babuška-Brezzi condition: A stable Petrov-Galerkin formulation of the Stokes problem accommodating equal-order interpolations, Comput. Methods Appl. Mech. Engrg. 59 (1) (1986) 85–99, http://dx.doi.org/10.1016/0045-7825(86)90025-3.
[6] M. Pastor, M. Quecedo, O.C. Zienkiewicz, A mixed displacement-pressure formulation for numerical analysis of plastic failure, Comput. Struct. 62 (1) (1997) 13–23, http://dx.doi.org/10.1016/S0045-7949(96)00208-8.
[7] J. Douglas, J.P. Wang, An absolutely stabilized finite element method for the stokes problem, Math. Comp. 52 (186) (1989) 495–508, http://dx.doi.org/10.1090/S0025-5718-1989-0958871-X.
[8] T.J. Hughes, A multidimentional upwind scheme with no crosswind diffusion, in: Finite element methods for convection dominated flows, Vol. 34, AMD, 1979.
[9] T.J. Hughes, A theoretical framework for Petrov-Galerkin methods with discontinuous weighting functions: Application to the streamline-upwind procedure, Finite Elem. Fluids 4 (1982) Chapter–3.
[10] L.P. Franca, T.J. Hughes, A.F. Loula, I. Miranda, A new family of stable elements for nearly incompressible elasticity based on a mixed Petrov-Galerkin finite element formulation, Numer. Math. 53 (1) (1988) 123–141, http://dx.doi.org/10.1007/BF01395881.
[11] O. Klaas, A. Maniatty, M.S. Shephard, A stabilized mixed finite element method for finite elasticity.: Formulation for linear displacement and pressure interpolation, Comput. Methods Appl. Mech. Engrg. 180 (1–2) (1999) 65–79, http://dx.doi.org/10.1016/S0045-7825(99)00059-6.
[12] A. Masud, K. Xia, A stabilized mixed finite element method for nearly incompressible elasticity, J. Appl. Mech. 72 (5) (2005) 711–720, http://dx.doi.org/10.1115/1.1985433.
[13] A. Truty, A Galerkin/least-squares finite element formulation for consolidation, Internat. J. Numer. Methods Engrg. 52 (8) (2001) 763–786, http://dx.doi.org/10.1002/nme.224.
[14] J.A. White, R.I. Borja, Stabilized low-order finite elements for coupled solid-deformation/fluid-diffusion and their application to fault zone transients, Comput. Methods Appl. Mech. Engrg. 197 (49–50) (2008) 4353–4366, http://dx.doi.org/10.1016/j.cma.2008.05.015.
[15] M. Preisig, J.H. Prévost, Stabilization procedures in coupled poromechanics problems: A critical assessment, Int. J. Numer. Anal. Methods Geomech. 35 (11) (2011) 1207–1225, http://dx.doi.org/10.1002/nag.951.
[16] H.T. Honório, C.R. Maliska, M. Ferronato, C. Janna, A stabilized element-based finite volume method for poroelastic problems, J. Comput. Phys. 364 (2018) 49–72, http://dx.doi.org/10.1016/j.jcp.2018.03.010.
[17] A. Franceschini, N. Castelletto, J.A. White, H.A. Tchelepi, Algebraically stabilized Lagrange multiplier method for frictional contact mechanics with hydraulically active fractures, Comput. Methods Appl. Mech. Engrg. 368 (2020) http://dx.doi.org/10.1016/j.cma.2020.113161.
[18] D. Moretto, A. Franceschini, M. Ferronato, A stabilized formulation for the mortar method with non-linear contact constraints, Appl. Math. 70 (6) (2025) 825–849, http://dx.doi.org/10.21136/AM.2025.0149-25.
[19] H.T. Honório, A. Franceschini, M. Ferronato, H. Hajibeygi, A machine learning-based stabilized finite element formulation for the mean stress computation in linear elasticity and coupled poroelasticity, Comput. Methods Appl. Mech. Engrg. 449 (2026) 118515, http://dx.doi.org/10.1016/j.cma.2025.118515.
[20] T.J. Hughes, Multiscale phenomena: Green's functions, the Dirichlet-to-Neumann formulation, subgrid scale models, bubbles and the origins of stabilized methods, Comput. Methods Appl. Mech. Engrg. 127 (1–4) (1995) 387–401, http://dx.doi.org/10.1016/0045-7825(95)00844-9.
[21] M. Cervera, M. Chiumenti, Q. Valverde, C.A. de Saracibar, Mixed linear/linear simplicial elements for incompressible elasticity and plasticity, Comput. Methods Appl. Mech. Engrg. 192 (49–50) (2003) 5249–5263, http://dx.doi.org/10.1016/j.cma.2003.07.007.
[22] M. Cervera, M. Chiumenti, C. Agelet de Saracibar, Softening, localization and stabilization: capture of discontinuous solutions in J2 plasticity, Int. J. Numer. Anal. Methods Geomech. 28 (5) (2004) 373–393, http://dx.doi.org/10.1002/nag.341.
[23] B. Ramesh, A.M. Maniatty, Stabilized finite element formulation for elastic–plastic finite deformations, Comput. Methods Appl. Mech. Engrg. 194 (6–8) (2005) 775–800, http://dx.doi.org/10.1016/j.cma.2004.06.025.
[24] N. Abboud, G. Scovazzi, Elastoplasticity with linear tetrahedral elements: A variational multiscale method, Internat. J. Numer. Methods Engrg. 115 (8) (2018) 913–955, http://dx.doi.org/10.1002/nme.5831.
[25] T.J.R. Hughes, Equivalence of finite elements for nearly incompressible elasticity, J. Appl. Mech. 44 (1) (1977) 181–183, http://dx.doi.org/10.1115/1.3423994.

[26] E. de Souza Neto, D. Perić, M. Dutko, D. Owen, Design of simple low order finite elements for large strain analysis of nearly incompressible solids, Int. J. Solids Struct. 33 (20–22) (1996) 3277–3296, http://dx.doi.org/10.1016/0020-7683(95)00259-6.
[27] B.Y. Park, B.L. Roberts, S.R. Sobolik, Construction of hexahedral finite element mesh capturing realistic geometries of a petroleum reserve, Finite Elem. Anal. Des. 135 (2017) 68–78, http://dx.doi.org/10.1016/j.finel.2017.07.007.
[28] H.T. Honório, H. Hajibeygi, Three-dimensional multi-physics simulation and sensitivity analysis of cyclic energy storage in salt caverns, Int. J. Hydrog. Energy 94 (2024) 1389–1405, http://dx.doi.org/10.1016/j.ijhydene.2024.11.081.
[29] C. Desai, A. Varadarajan, A constitutive model for quasi-static behavior of rock salt, J. Geophys. Res.: Solid Earth 92 (B11) (1987) 11445–11456, http://dx.doi.org/10.1029/JB092iB11p11445.
[30] H.T. Honório, M. Houben, K. Bisdom, A. van der Linden, K. de Borst, L.J. Sluys, H. Hajibeygi, A multi-step calibration strategy for reliable parameter determination of salt rock mechanics constitutive models, Int. J. Rock Mech. Min. Sci. 183 (2024) 105922, http://dx.doi.org/10.1016/j.ijrmms.2024.105922.
[31] E.G. Kirsch, Die theorie der elastizit t und die bed rfnisse der festigkeitslehre, Zeitshrift Des Vereines Dtsch. Ingenieure 42 (1898) 797–807.